Selecting CMIP6 GCMs for CORDEX Dynamical Downscaling over Southeast Asia Using a Standardised Benchmarking Framework

Phuong Loan Nguyen[1,2], Lisa V. Alexander[1,2], Marcus J. Thatcher[3], Son C. H. Truong[3], Rachael N. Isphording[1,2], John L. McGregor[3]

[1]ARC Centre of Excellence of Climate Extremes and Climate Change Research Centre, UNSW Sydney, Sydney, NSW 2052, Australia
[2]ARC Centre of Excellence for the Weather of the 21st Century, UNSW Sydney, Sydney, NSW 2052, Australia
[3]CSIRO Environment, Commonwealth Scientific and Industrial Research Organisation, Aspendale, Victoria

Correspondence to: Phuong Loan Nguyen (phuongloan.nguyen@unsw.edu.au)

Abstract. Downscaling global climate models (GCMs) provides crucial, high-resolution data needed for informed decision-making at regional scales. However, there is no uniform approach to select the most suitable GCMs. Over Southeast Asia (SEA), observations are sparse and have large uncertainties, complicating GCM selection especially for rainfall. To guide this selection, we apply a standardised benchmarking framework to select CMIP6 GCMs for dynamical downscaling over SEA, addressing current observational limitations. This framework identifies fit-for-purpose models through a two-step process: (a) selecting models that meet minimum performance requirements in simulating the fundamental characteristics of rainfall (e.g., bias, spatial pattern, annual cycle, and trend) and (b) selecting models from (a) to further assess whether key precipitation drivers (monsoon) and teleconnections from modes of variability are captured [El Niño-Southern-Oscillation (ENSO) and Indian Ocean Dipole (IOD)]. GCMs generally exhibit wet biases, particularly over the complex terrain of the Maritime Continent. Evaluations from the first step identify 19 out of 32 GCMs that meet our minimum performance expectations in simulating rainfall. These models also consistently capture atmospheric circulations and teleconnections with modes of variability over the region but overestimate their strength. Ultimately, we identify eight GCMs meeting our performance expectations. There are obvious, high-performing GCMs from allied modelling groups, highlighting the dependency of the subset of models identified from the framework. Therefore, further tests on model independence, data availability, and future climate change spread are conducted, resulting in a final sub-set of two independent models that align with our a priori expectations for downscaling over CORDEX-SEA.

Keywords: CORDEX, regional climate models, CMIP6, standardised benchmarking framework, GCM selection.

1 Introduction

The Sixth Assessment Report (AR6) of the Intergovernmental Panel on Climate Change (IPCC) underscores, with high confidence, the escalating water-related risks, losses and damages associated with each increment of global warming (Ipcc, 2023). The report specifically notes a projected increase in the frequency and intensity of heavy rainfall, leading to an increased risk of rain-generated localised flooding, particularly over coastal and low-lying cities and regions [Section 3 (Ipcc, 2023)]. Therefore, climate projections at regional scales are required to inform climate change adaptation strategies and enhance resilience efforts.

Different types of models have been developed and have become fundamental tools for assessing future regional climate changes, including state-of-the-art Global Climate Models (GCMs) and Regional Climate Models (RCMs). GCMs are generally used to explore climate interactions and underpin climate projections through the Coupled Model Intercomparison Project [CMIP ; (Meehl et al., 2000)], an initiative of the World Climate Research Programme (WCRP). However, with a typical horizontal resolution of 50-250 km, GCMs have limited ability to simulate sub-grid weather (e.g., local variance, persistence, topography, etc.) and therefore cannot accurately define local-scale processes and feedbacks (e.g., deep convection, land-atmosphere interactions, etc.). This limits GCMs' ability to simulate aspects of the present-day water cycle and to determine robust future changes for local and regional applications (Maraun and Widmann, 2018; Douville et al., 2021). RCMs dynamically downscale GCM outputs to create higher spatial resolutions of ~2 -50 km, providing richer regional spatial information (e.g., small-scale processes and extreme events) for climate assessments and for impact and adaptation studies (Diaconescu and Laprise, 2013; Giorgi and Gao, 2018). However, such experiments are computationally expensive, so it is not practical to choose all GCMs for dynamical downscaling. Thus, a sub-set of GCMs has to be selected.

The WCRP's Coordinated Regional Climate Downscaling Experiment (Cordex) initiative delivers dynamically downscaled simulations of various GCMs (Giorgi and Gao, 2018) over 14 regions worldwide. This includes Phase I using CMIP5 (Giorgi et al., 2008) and Phase II Coordinated Output for Regional Evaluations (CORDEX-CORE) (Giorgi et al., 2021) as well as on-going experiments (CMIP6). However, there is no agreed approach to selecting which GCMs would be most suitable for dynamical downscaling, either in the recent WCRP's guideline for CMIP6 CORDEX experiments (Cordex, 2021) or across different CORDEX domains (Di Virgilio et al., 2022; Grose et al., 2023; Sobolowski et al., 2023). In the earliest initiatives, GCMs were eliminated based on their skill in reproducing the current climate for the region of interest given the fact that the bias in the GCMs can propagate into the RCM through the underlying and lateral boundary conditions (i.e., driven by initial and time-dependent meteorological variables from GCMs) (Mote et al., 2011; Overland et al., 2011; Mcsweeney et al., 2012; Mcsweeney et al., 2015). In addition, the selection of GCMs considers the need to generate a reasonable uncertainty range for future climate projections (Mote et al., 2011; Overland et al., 2011). Given the shared physical components of the design of CMIP6 GCMs, there are inherent biases in statistical properties like the multi-model mean or standard deviation of the full ensemble (Boé, 2018; Brands, 2022; Sobolowski et al., 2023). To address this problem, model dependency is also considered. These considerations and methodologies have been integrated into the most recent CMIP6 CORDEX experimental design for specific regions, such as Europe (Sobolowski et al., 2023) or Australia (Di Virgilio et al., 2022) and are recommended for widespread application across other CORDEX-domains.

69   Model evaluation is an essential part of CMIP6 model selection since simulating past performance well is a
70   necessary (but insufficient) condition to have more confidence in future performance. Different metrics are
71   employed to quantify model skill in simulating various climate variables at either global (Kim et al., 2020; Ridder
72   et al., 2021; Wang et al., 2021b; Donat et al., 2023) or regional scales [e.g., Australia (Deng et al., 2021; Di
73   Virgilio et al., 2022) Europe (Ossó et al., 2023; Palmer et al., 2023); South America (Díaz et al., 2021); Asia
74   (Dong and Dong, 2021); Southeast Asia (Desmet and Ngo-Duc, 2022; Pimonsree et al., 2023)]. However, the lack
75   of consistency in the list of metrics used makes it difficult to perform one-to-one comparisons between studies or
76   to track model performance across various regions.

77   Recently, Isphording et al. (2024) introduced a standardised benchmarking framework (BMF) underpinned by the
78   work of the U.S DOE (2020), which included a set of baseline performance metrics for assessing model
79   performance in simulating different characteristics of rainfall. The BMF is different from traditional model
80   evaluation in that it defines performance expectations a priori (Abramowitz, 2005; Abramowitz, 2012; Best, 2015;
81   Nearing et al., 2018). Under the BMF, a model will not be considered fit-for-purpose if it fails any performance
82   metric. The BMF consists of two tiers of metrics: the first tier includes minimum standard performance metrics
83   related to fundamental characteristics of rainfall, and the second tier allows users to define metrics that help to
84   answer specific scientific research questions. The BMF was initially designed for rainfall but can be widely
85   applied to other climate variables (e.g., surface temperature), depending on the user's purpose (Isphording et al.,
86   2024).

87   IPCC highlights Southeast Asia (SEA) as a region facing considerable climate change risks from extreme events
88   (e.g., floods, extreme heat, and changing precipitation and extremes) (Ipcc, 2022). However, available regional
89   climate simulations for SEA, particularly from CMIP5 CORDEX-SEA experiments are limited to 13 simulations
90   (Tangang et al., 2020) compared to EURO-CORDEX with 68 simulations (Jacob et al., 2020) or CORDEX-
91   Australasia with 20 simulations (Evans et al., 2021). Consequently, future projections come with a higher degree
92   of uncertainty, especially for rainfall (Tangang et al., 2020; Nguyen et al., 2023). This motivated the CORDEX-
93   SEA community to update their regional climate model simulations with the latest CMIP6 models. Note that over
94   SEA, observations are sparse with large uncertainties, particularly for rainfall (Nguyen et al., 2020), making GCM
95   evaluations more complicated (Nguyen et al., 2022; Nguyen et al., 2023). To date, the performance of various
96   CMIP6 GCMs has been evaluated and ranked over the whole region of SEA (Desmet and Ngo-Duc, 2022;
97   Pimonsree et al., 2023) and its sub-regions [e.g., Philippines (Ignacio-Reardon and Luo, 2023); Thailand
98   (Kamworapan et al., 2021); Vietnam (Nguyen-Duy et al., 2023)]. Although there are groups of GCMs that
99   consistently perform well (e.g., EC-Earth3, EC-Earth3-Veg, GFDL-ESM4, MPI-ESM1-2-HR, E3SM1-0,
100   CESM2) and poorly (e.g., FGOALS-g3, CanESM, NESM3, IPSL-CM6A-LR) across available literature, their
101   ranking varies differently given inconsistencies in evaluation metrics and observational reference datasets. This
102   creates challenges in conducting direct intercomparisons across the above-mentioned studies. In addition, it is
103   crucial to consider other important aspects discussed above (e.g., observational uncertainty, model dependency,
104   and future climate change spread) in identifying the list of reliable models over SEA.

105   In this research, we aim to apply the lessons learnt from CMIP6 selection over different CORDEX-domains for
106   SEA by assessing different aspects of models: model performance, model independence, data availability and
107   future climate change spread. We apply the BMF to provide a consistent set of metrics for holistically evaluating

108 model performance and to deal with large observational uncertainties over the region. Focusing on precipitation,
109 where future projections are much more uncertain, the objectives of this research are twofold:

110   1. To evaluate the performance of CMIP6 GCMs in simulating the fundamental characteristics of
111   precipitation, its drivers and teleconnection with modes of variability over SEA using a standardised
112   benchmark framework and to identify a subset of models that meet our performance expectations.
113   2. To retain models that are relatively independent and are representative of the full range of possible
114   projected change for finalizing a subset of CMIP6 GCMs for dynamical downscaling over SEA using
115   model independence tests and assessment of climate change response patterns.

116 The structure of the paper is as follows: Section 2 introduces the data and the benchmarking framework employed
117 in this study. The results are presented in three subsections: Section 3.1 focuses on model assessment using the
118 benchmarking framework; Section 3.2 examines the spread of future climate change among models; and Section
119 3.3 assesses model dependence through cluster analysis. Finally, we conclude with a discussion of our results in
120 Section 4 and a summary of the main conclusions in Section 5.

121 **2 Methods**

122 **2.1 Data**

123 **2.1.1 CMIP6 GCM data**

124 We use the historical daily data of precipitation, near surface temperature, 850 hPa wind speed and both monthly
125 and daily sea-surface temperature data from the 32 CMIP6 models listed in Table 1. We consider only models
126 which have a horizontal grid spacing finer than $2° \times 2°$ which are likely to be more suitable for dynamical
127 downscaling. One simulation (typically the first member r1i1f1p1) is utilized in the benchmarking process to
128 enable a fair comparison. At the time of this analysis, the first member of some models (e.g., CNRM-family
129 models, UKESM1-0-LL and HadGEM3-GC31-MM) was not available so another member was utilized.

130 **Table 1.** Information on model components from the CMIP6 GCMs used in this study.

No	Model	Run	Atmosphere lon/lat	Reference	Atmospheric component	Land component	Sea ice component	Ocean component
1	ACCESS-CM2*	r1i1p1f1	1.2° × 1.8°	Bi et al. (2020) and Ziehn et al. (2020)	UKMO UM v10.6	CABLE 2.5	LANL CICE5.1	MOM5
2	ACCESS-ESM1-5*	r1i1p1f1	1.2° × 1.8°		UKMO UM V7.3	CABLE2.4	LANL CICE4.1	GFDL MOM5
3	BCC-CSM2-MR*	r1i1p1f1	1.1° × 1.1°	Wu et al. (2019)	BCC-AGCM3	BCC-AVIM2	SIS4	MOM4-L40
4	CESM2*	r1i1p1f1	0.95° × 1.25°	Danabasoglu et al. (2020)	CAM6/WACCM6	CLM5.0	CICE5	POP2
5	CMCC-CM2-HR4	r1i1p1f1	0.95° × 1.25°	Cherchi et al. (2019)	CAM v5	CLM4.5	CICE4	NEMO v3.6
6	CMCC-CM2-SR5*	r1i1p1f1	0.9° × 0.9°					
7	CMCC-ESM2*	r1i1p1f1	0.95° × 1.25°					

No	Model	Run	Atmosphere lon/lat	Reference	Atmospheric component	Land component	Sea ice component	Ocean component
8	CNRM-CM6-1*	r1i1p1f2	1.4° × 1.4°	Voldoire et al. (2019)	ARPPE-Climat v6.3	Flake	OASIS-MCT	NEMO
9	CNRM-CM6-1-HR	r1i1p1f2	0.5° × 0.5°					
10	CNRM-ESM2-1*	r1i1p1f2	1.4° × 1.4°					
11	E3SM-1-0*	r1i1p1f1	1° × 1°	Zheng et al. (2022)	EAM (CAM 5.3)	MPAS-Ocean	MPAS-Seaice	ELMv0 (CLM4.5)
12	EC-Earth3-AerChem	r1i1p1f1	0.7° × 0.9°	Döscher et al. (2022)	ECMWF IFS	LPJ-GUESS et al., 2013)	LIM3	NEMO v3.6
13	EC-Earth3-CC	r1i1p1f1	0.7° × 0.9°					
14	EC-Earth3*	r1i1p1f1	0.7° × 0.7°					
15	EC-Earth3-Veg*	r1i1p1f1	0.7° × 0.7°					
16	EC-Earth3-Veg-LR	r1i1p1f1	1.125° × 1.125°					
17	GFDL-CM4	r1i1p1f1	1.0° × 1.3°	Held et al. (2019); Dunne et al. (2020)	AM4	LM4	SIS 2	OM4 MOM6
18	GFDL-ESM4*	r1i1p1f1	1.0° × 1.3°					
19	HadGEM3-GC31-MM	r1i1p1f3	0.9° × 0.9°	Andrews et al. (2020)	GA7/GL7		GSI8.1 (CICE5.1)	GO6 (NEMO)
20	INM-CM4-8	r1i1p1f1	1.5° × 2.0°	Volodin et al. (2017)	INM-AM4-8/5.0	INM-LND1	INM-ICE1	INM-OM5
21	INM-CM5-0	r1i1p1f1	1.5° × 2.0°					
22	IPSL-CM6A-LR*	r1i1p1f1	1.3° × 2.5°	Boucher et al. (2020)	LMDZ 6A-LR	ORCHIDE 2.0	NEMO-LIM3.6	NEMO 3.6
23	IPSL-CM6A-LR-INCA*	r1i1p1f1	1.27° × 2.5°					
24	MIROC6*	r1i1p1f1	1.4° × 1.4°	Tatebe et al. (2019)	MIROC 3.2	MATSIRO	MIROC 3.2	COCO 4.5
25	MPI-ESM1-2-HR*	r1i1p1f1	0.94° × 0.94°	Mauritsen et al. (2019)	ECHAM6.3	JSBACH)	MPIOM	
26	MPI-ESM1-2-LR*	r1i1p1f1	1.875° × 1.875°					
27	MRI-ESM2-0*	r1i1p1f1	1.1° × 1.1°	Yukimoto et al. (2019)	MRI-AGCM3.5		MRI.COMv4	
28	NESM3	r1i1p1f1	1.9° × 1.9°	Cao et al. (2018)	ECHAM6.3	JSBACH	CICE4	NEMO v3.4
29	NorESM2-MM*	r1i1p1f1	0.9 × 0.9°	Seland et al. (2020)	CAM4-Oslo	CLM4	CICE4	MICOM
30	SAM0-UNICON*	r1i1p1f1	0.9° × 1.3°	Park et al. (2019)	CAM5.3 with UNICON	CLM4	CICE4.0	POP2
31	TaiESM1*	r1i1p1f1	0.9° × 0.9°	Wang et al. (2021a)	Tai AM1	CLM4.0	CICE4	POP2
32	UKESM1-0-LL*	r1i1p1f2	1.3° × 1.9°	Sellar et al. (2019)	MetUM-HadGEM3-GA7.1	JULES-ES-1.0	CICE-HadGEM3-GSI8	NEMO-HadGEM3-GO6.0

131 *Model offers atmospheric variables available in three dimensions at each 6 hours for dynamical downscaling at
132 the time of analyses.

133

 2.1.2 Observations and reanalyses

135 Given the large observational uncertainty in precipitation over the region (Nguyen et al. 2022), we use multiple

136 daily observed datasets from different in situ and satellite sources to quantify model skill (Table 2). These datasets

137 have been chosen given their high consistency in representing daily precipitation (Nguyen et al., 2022) and

138 extremes (Alexander et al., 2020; Nguyen et al., 2020) over SEA.

139 ERA5 reanalysis (~31 km grid resolution) (Hersbach et al., 2020) was used to benchmark model performance in

140 representing the climatology of atmospheric circulation (e.g., metrics related to horizontal wind at 850 hPa level

141 are described in section 2.2).

142 We acknowledge that different observational sea surface temperatures (SST) have different abilities to capture

143 signals of the modes of variability. Therefore, we utilize multiple SST products (Table 2) to take account of the

144 observational uncertainties in simulating the teleconnection between rainfall and main modes of variability,

145 including El Niño-Southern Oscillation (ENSO) and Indian Ocean Dipole (IOD) as described in section 2.2.

146 **Table 2.** The main characteristic of observational datasets used in this study.

Type of dataset	Product short name	Dataset name	Temporal coverage	Spatial resolution	Data source	Reference
Precipitation dataset	APHRODITE	APHRODITE V1101 and V1101XR	1950-2015	0.5° × 0.5°	In situ	Yatagai et al. (2012)
	CHIRPv2	CHIRPSv2	1981-2016	0.25° × 0.25°	In situ + Satellite	Funk et al. (2015)
	REGEN_ALL	REGEN Allstns V1 2019	1950-2019	1° × 1°	In situ	Contractor et al. (2020)
	GPCC_v2018	GPCC FDD v2018	1982-2019	1° × 1°	In situ	Schamm et al. (2014)
Sea Surface Temperature dataset	HadISST	HadISST1 v1	1870-2021	1° × 1°	In situ + Satellite	Rayner et al. (2003)
	OISST	OISST v2.0	1981-2020	0.25° × 0.25°	In situ + Satellite	Huang et al. (2021)
	ERSST	ERSST v5	1854-2024	2° × 2°	In situ	Huang et al. (2017)

147 **2.2 Benchmarking CMIP6 GCMs over Southeast Asia**

148 Given the large uncertainties and model inconsistency in rainfall projections, our main aim is to identify a subset

149 of CMIP6 GCMs that meet our a priori expectations. That is, as a minimum requirement a model should simulate

150 past rainfall statistics over SEA reasonably well using consistent criteria. Figure 1 illustrates the GCM selection

151 process applied in this research based on a standardised benchmarking framework (Isphording et al., 2024). A

152 subset of CMIP6 GCMs that meet our model performance expectations are identified through a two-step process:

153 (a) selecting models that meet minimum performance requirements in simulating the fundamental characteristics

154 of rainfall (Fig. 1) and (b) selecting models from (a) to further assess performance in simulating precipitation

155 drivers (e.g., monsoon) and teleconnections with modes of variability (Fig. 1).

2.2.1 Minimum standard metrics

The BMF introduces a set of minimum-standard metrics (MSMs): 1. mean absolute percentage error (MAPE), 2. spatial correlation (Scor), 3. seasonal cycle (Scyc) and 4. significant changes (SigT) (Isphording et al., 2024) to assess the skill of climate models in simulating very fundamental characteristics of precipitation (e.g., magnitude of biases, spatial distributions, annual cycles and temporal variability). Before exploring complex processes, a model should meet performance expectations for these MSMs. Therefore, we initially calculate the MSMs for precipitation. In addition, we acknowledge that models should produce adequate present-day simulations of other fundamental climate variables like near-surface temperature. Hence, we also apply the MSMs for near-surface temperature in the supplementary information. Given the strong seasonality of precipitation in the region (Juneng et al., 2016), the analyses related to precipitation are conducted at a seasonal scale (e.g., the dry season November-April – NDJFMA and the wet season May-October – MJJASO). Meanwhile, temperature analyses are conducted at the annual scale.
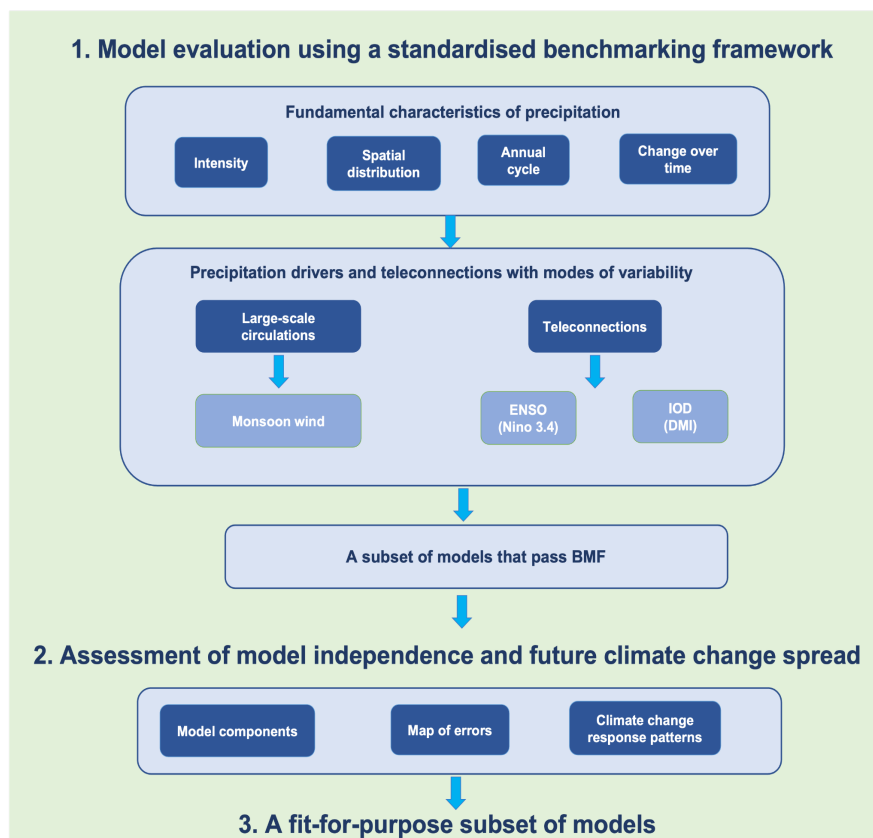
Figure 1. A schematic of the CMIP6 GCM selection process, including (1) model evaluation using a standardized benchmarking framework (BMF) and (2) assessment of model independence and future climate change spread. The BMF includes two steps: minimum standard metrics (MSMs) which assess very basic characteristics of rainfall and second-tier metrics (e.g., versatility metrics) which quantify model skill of the models that pass the MSMs in simulating precipitation drivers (monsoon) and teleconnections with modes of variability [the El Niño-Southern Oscillation (ENSO) and Indian Ocean Dipole (IOD)].

175 Note that in this research, we focus only precipitation over land given the lack of in situ reference over ocean.

176 Some satellite-derived products provide oceanic precipitation data but most of their temporal coverage is not

177 sufficiently long to use as a reference. In addition, the observational uncertainties among satellite clusters in

178 estimating oceanic precipitations over SEA is quite substantial, with discrepancies reaching up to 4 mm/day

179 (Figure s1).

180 **2.2.2 Versatility metrics**

181 The MSMs provide statistical measurements that are not always correlated with future projections (Knutti et al.,

182 2010), given that some models may simulate historical precipitation well for the wrong reasons. A further

183 recommendation is therefore to also assess model performance based on key physical processes (Doe, 2020;

184 Nguyen et al., 2023). This approach offers additional insights into the relative roles of model biases in simulating

185 large-scale environments versus the limitations of model parameterizations in generating precipitation biases.

186 Therefore, we define second tier versatility metrics to assess those GCMs selected from section 2.2.1 in simulating

187 the complex precipitation-related processes, including drivers and teleconnections with modes of variability.

188 **Monsoon circulation**

189 SEA is situated within the Asian monsoon regime, where atmospheric circulation is modulated by two primary

190 monsoon systems: the Indian monsoon characterized by westerlies from the Bay of Bengal into northern parts of

191 SEA including the mainland and northern Philippines (along 10°N) during the boreal summer (JJAS) and reversed

192 in direction during the boreal winter (DJF); and the Australian monsoon [e.g., easterlies from Australia to the

193 Maritime Continent (MC) and Papua] (Chang et al., 2005). These monsoon systems drive regional rainfall

194 seasonality. Therefore, we focus on assessing model skill in simulating the intensity and direction of monsoon

195 wind (e.g., 850-hPa wind) for JJAS and DJF. While wind speed is evaluated using the MAPE and Scor metrics

196 similar to the MSMs for precipitation and temperature, wind direction is quantified using an equation from Desmet

197 and Ngo-Duc (2022):

198 $$MD = \frac{\sum_i u_i \times \left| \theta_i - \theta_{i,ref} \right|_{[0,180]}}{\sum_i u_i}$$

199 where u_i refers to the simulated wind speed at the grid i, θ_i and $\theta_{i,ref}$ are the wind direction at grid i in the

200 simulated and reference data respectively. $\left| \theta_i - \theta_{i,ref} \right|_{[0,180]}$ is the absolute value of difference at the ith grid

201 between directions of simulated and reference wind speed (e.g., ERA5). The MD metric allows us to quantify the

202 agreement in wind direction between two datasets in which the impact of high wind speed is taken into account.

203 **ENSO, IOD and Teleconnections**

204 Various parts of SEA are also affected by two prominent modes of variability: the El Niño - Southern Oscillation

205 (ENSO) (Haylock and Mcbride, 2001; Chang et al., 2005; Juneng and Tangang, 2005; Qian et al., 2013) and

206 Indian Ocean Dipole (IOD) (Xu et al., 2021) via atmospheric teleconnections. In this research, the teleconnection

207 is defined by the temporal correlation between precipitation anomalies at each grid point and the ENSO/IDO

208 indices.

209   To track ENSO variability, the Niño3.4 index (5°S-5°N and 160°E-120°W) (Trenberth and Hoar, 1997; Shukla et

210   al., 2011) derived for the 1951-2014 period as area-mean monthly SST anomalies with respect to a 1961-1990

211   climatology is used. For IOD, we use the Dipole Mode Index [DMI; (Saji et al., 1999; Meyers et al., 2007)] DMI

212   measures differences of monthly SST anomalies between the west equatorial Indian Ocean (50-70° E, 10°S-10°N)

213   and those in the east (90-110°S, 10°S -0°N).

214   We use a 5-monthly average Niño3.4 and IOD index to remove seasonal cycles. The resulting monthly time series

215   are detrended using a fourth-order polynomial fit to remove the possible influence of a long-term trend and to

216   better preserve high amplitude (<10 years) variability (Braganza et al., 2003).

217   Since ENSO typically matures toward the end of the calendar year (Rasmusson and Carpenter, 1982), we consider

218   ENSO developing years as year (0) and use the DJF means to identify ENSO events. Over SEA, ENSO interacts

219   with the monsoon cycle and due to the varying monsoon onset between the northern and southern parts of the

220   region, its seasonal evolution differs across regions (Figure s2). In particular, there is a lagged negative correlation

221   between rainfall and ENSO over the Maritime Continent (MC) and the Philippines, which develops from May-

222   June, strengthens during July-August, and reaches its highest correlation during September-October of the

223   developing year (year 0). On the other hand, this negative correlation becomes prominent over the northern parts

224   during the subsequent boreal spring (from March-May of the year +1) (Wang et al., 2020; Chen et al., 2023). The

225   negative correlation indicates dry anomalies during El Niňo and/or wet anomalies during La Nina. Therefore, in

226   the context of this research, we examine the lead/lag Pearson correlation of the DJF Niño3.4 index in the

227   developing year (year 0) with two different seasonal rainfalls: May-Oct (MJJASO) of the developing year (year

228   0) and March-May (MAM) of the following year (year +1).

229   Furthermore, considering the stronger influence of the IOD and its associated teleconnection during SON

230   compared to other seasons (Mckenna et al., 2020), we calculated the in-phase Pearson correlation coefficient

231   between the detrended precipitation anomaly and DMI for the SON season. The statistical significance of the

232   correlation coefficient is tested using the Student t-test (alpha = 0.05). Note that IOD could exist as part of ENSO

233   (Allan et al., 2001; Baquero-Bernal et al., 2002) and their coexistence could have strong impacts on rainfall

234   variability over many parts of SEA (D'arrigo and Wilson, 2008; Amirudin et al., 2020), which is not investigated

235   in this study.

236   Previous literature has often focused on assessing the robustness of rainfall teleconnections (e.g., spatial patterns

237   and amplitudes) across CMIP model ensembles. These assessments typically involve examining agreement in the

238   sign of teleconnections such as through rainfall anomaly composites (Langenbrunner and Neelin, 2013) and

239   regional average teleconnection strength over land (Perry et al., 2020) or a combination of both (Power and

240   Delage, 2018) rather than evaluating the skill of an individual model. However, since rainfall teleconnections

241   across SEA exhibit spatial and seasonal variability, the above metrics may be substantially influenced by internal

242   variability. For high level qualification, we employ spatial correlation and simplified metrics to assess whether

243   there are significant correlations teleconnections as recommended by Liu et al. (2024). We assess the similarity

244   in the number of grid points detecting significant signals between observed and modelled teleconnections using a

245   set of three metrics: Hit rate (HR), Miss Rate (MR) and False Alarm rate (FAR) as follows:

246    $$\text{HR} = \frac{Area\ with\ correct\ sign\ of\ significant\ correlation}{Area\ with\ significant\ correlation\ in\ OBS}$$

247 $$\text{MR} = \frac{Area\ with\ significant\ correlation\ in\ OBS\ but\ with\ no\ significant\ correlation\ in\ model}{Area\ with\ significant\ correlation\ in\ OBS}$$

248 $$\text{FAR} = \frac{Area\ with\ no\ significant\ correlation\ in\ OBS\ but\ with\ significant\ correlation\ in\ model}{Area\ with\ no\ significant\ correlation\ in\ OBS}$$

249 These metrics allow us to make sure that the model adequately simulates significant signals across the entire
250 region. While HR ranges from 0-1, MR and FAR vary. A desirable model outcome includes a high HR value
251 coupled with a low MR and FAR value, indicating the model's ability to adequately capture the significance of
252 the correct signal in the right region (on grid scales) of teleconnections between ENSO and IOD and rainfall
253 pattern.

2.3. GCM independence assessment and future climate change spread

255 Model independence could be assessed based on model components (e.g., shared atmospheric, land, and/or ocean
256 models) and/or model output patterns. In this study, we employ both methods for testing GCM independence.
257 Table 1 provides information on the principal components of the models used in this study. Note that model
258 independence based on this criterion could depend on the model version (e.g., the same model with different levels
259 of complexity). In addition, we acknowledge that the spatial pattern of error maps and future changes maps seem
260 to correlate well with model dependency (Knutti et al., 2010; Knutti and Sedláček, 2013; Brunner et al., 2020;
261 Brands, 2022). Therefore, we determine the independence of GCMs simply by calculating the correlation
262 coefficient of historical biases and future projections between models and then apply a hierarchical clustering
263 approach (Rousseeuw, 1987) to this correlation matrix to group models. This cluster analysis has been employed
264 in previous literature for multiple purposes, e.g., to assess model dependency (Brunner et al., 2020; Masson and
265 Knutti, 2011), spatial patterns of climatology and trends in climate extremes (Gibson et al., 2017) or spatial pattern
266 of precipitation change signals (Gibson et al., 2024).

267 Note that historical biases are calculated by comparing the climatology of total rainfall over the land area of SEA
268 for the 1951-2014 period with corresponding data from an observed reference. Meanwhile, for future signals, we
269 focus on the relative change (in percentage) between the far future (2070-2099) and the baseline (1961-1990) as
270 suggested by the World Meteorological Organization (WMO). All analyses are conducted for two seasonal
271 periods: wet MJJASO and dry NDJFMA seasons.

272 We use the coarsest resolution (i.e., NESM ~216 km or 1.9°×1.9° resolution) among 32 GCMs as the target
273 resolution for comparison. All data are interpolated into a spatial resolution of 1.9°×1.9° using a first-order
274 conservative regridding method (Jones, 1999) to better capture the spatial discontinuity of precipitation
275 ((Contractor et al., 2018).

276 Benchmarking CMIP6 GCMs against observations is conducted over land for precipitation and the
277 teleconnections between precipitation and modes of variability while 850-hPa winds from ERA5 allow the
278 comparison to also be extended over the ocean.

279 Hereafter, we select APHRODITE as the primary baseline for all the main figures, as it utilises the greatest number
280 of rain gauges of any dataset. We include the results related to all other observational datasets in the
281 Supplementary section (Fig. s3-8) and provide a detailed explanation of related results in the main text for
282 intercomparison purposes.

3 Results

3.1 Minimum Standard Metrics (MSMs)

3.1.1 Mean absolute percentage error (MAPE) and Spatial correlation (Scor)

We initially assess the performance of CMIP6 GCMs in reproducing the spatial distribution of precipitation, using the first two MSMs: MAPE and Scor. Previous studies have emphasized strong seasonal and regional contrasts in rainfall distribution over Southeast Asia (Nguyen et al., 2023). Therefore, we focus on comparing the seasonal climatology (1951-2014) of total rainfall during wet days (e.g., precipitation ≥ 1mm) between models and APHRODITE for both wet MJJASO and dry NDJFMA seasons (Fig. 2 and Fig. 3 respectively). For MSMs, our strategy is to retain as many models as possible. We establish benchmarking thresholds based on the requirements of downscaling CMIP6 from CORDEX communities and our understanding of reasonable model performance based on current scientific understanding. In particular, GCMs should adequately produce the spatial distribution of rainfall and without a strong wet or dry bias. In addition, we also identify observational uncertainties through inter-comparison of multiple precipitation datasets. Considering variations in model performance across seasons, we also set different thresholds for benchmarking models for different seasons. In particular, due to a better model's ability to capture spatial variability of precipitation during the dry season compared to the wet season (Desmet and Ngo-Duc, 2022), we adopt a more lenient approach by relaxing our expectation for a spatial distribution metric, setting the Scor threshold ≥ 0.4 for the wet season and ≥ 0.75 for the dry season. However, for the MAPE score, we apply a stricter criterion, as we require models to closely simulate observed rainfall intensity over SEA. For both wet and dry seasons, we set the benchmarking threshold for MAPE at ≤ 0.75. With this threshold, our objective is to identify models capable of capturing the spatial variability of rainfall across at least 40% (Scor ≥ 0.4) or 75% (Scor ≥ 0.75) of the domain during wet and dry seasons respectively, with a wet/dry bias of no more than 75% compared to observations (MAPE ≤ 0.75) for both seasons.

We first discuss key features of the wet season (MJJASO; Fig. 2). Models are ranked from wettest to driest based on their regionally-averaged climatologies (i.e., the average of accumulated precipitation over all land grid points inside the domain). Models that meet our benchmarking thresholds for MAPE and Scor (i.e., calculated against APHRODITE) are highlighted by purple-coloured boxes. In general, CMIP6 GCMs demonstrate a wet bias in terms of regional averages, ranging from 6.32 mm/year to 131.78 mm/year except for MPI-ESM1-2-LR (-1.29 mm/year). However, there is spatial variability in the distribution of wet and dry biases. While most of these models consistently show wet biases over MC, dry biases are observed in different locations on the mainland across models [e.g., along the west coast (e.g., EC-Earth, IPSL and CMCC families) or east coast (e.g., CNRM family) as well as in some northern regions (e.g., MPI family)]. Among the wettest GCMs, including INM, IPSL, NorESM2-MM and CESM2 family, the largest biases are predominantly over MC. Interestingly, most CMIP6 GCMs can capture the spatial variability of rainfall (Scor is around or greater than 0.5), except for the IPSL-family simulations (Scors of 0.11 and 0.13). Using the threshold definitions mentioned above, six models fail to meet these benchmarks, exhibiting obvious grouping by GCM group. For example, IPSL-CM6A-LR and IPSL-CM6A-LR-INCA fail due to their low Scor (0.13 and 0.11 respectively) and high MAPE (1.20 and 1.26 respectively). While INM-CM5-0 and INM-CM4-8 models meet our set expectation in relation to spatial variability, they fail to meet the MAPE threshold due to their overestimation of rainfall across the entire region (e.g., MAPE ranging

321 from 1.29 to 1.38 respectively). All mentioned failed models exhibit high MAPE values, ranging from 0.81 to
322 1.28.
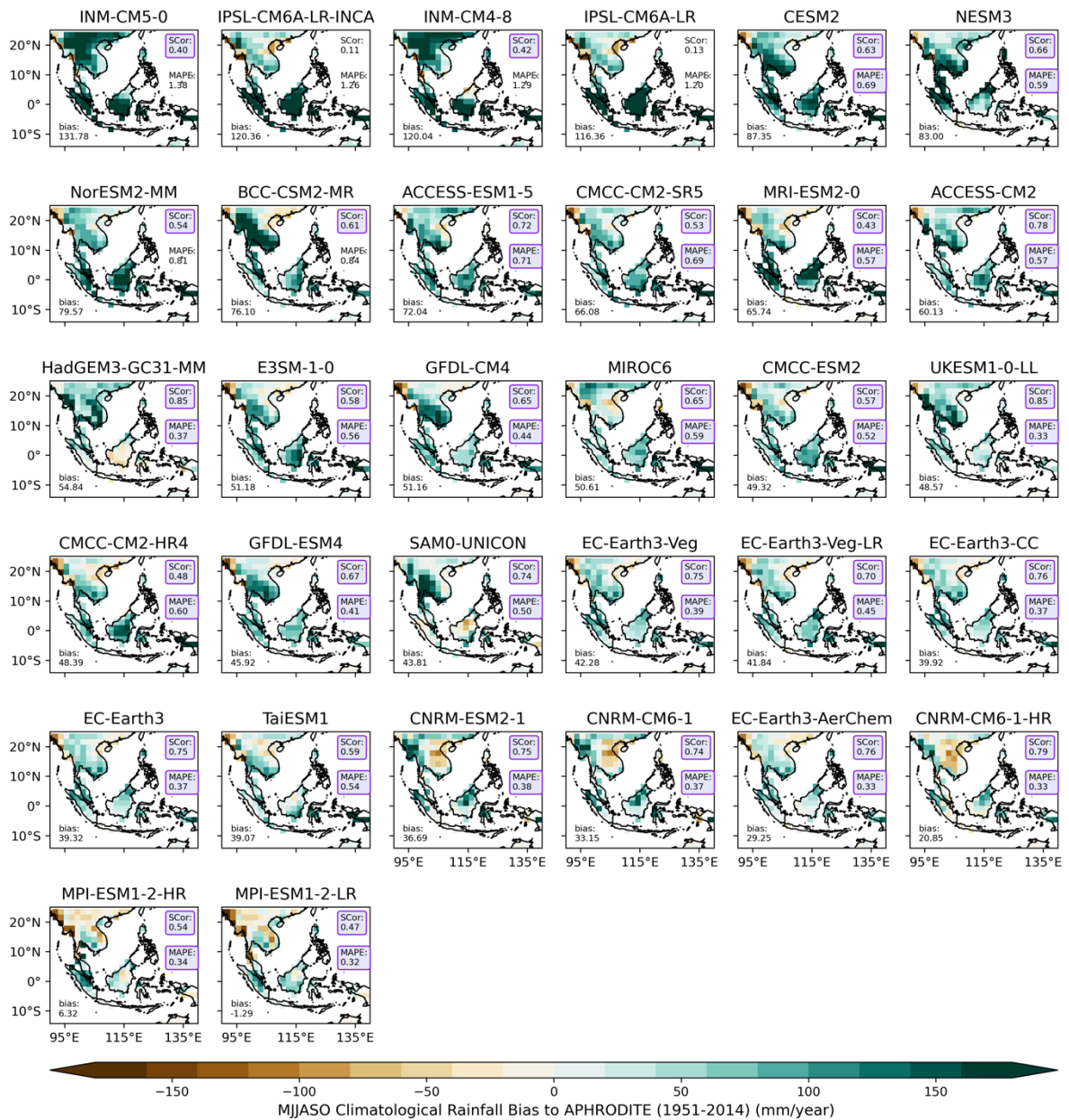
Figure 2. The seasonal climatological (1951-2014) bias (in mm/year) for each model against the APHRODITE observational product during the wet season (May-October; MJJASO), ranked wettest to driest based on regionally-averaged bias. The mean absolute percentage error (MAPE) and spatial correlation (Scor) calculated against APHRODITE are shown in the upper right corner. Values highlighted in purple-coloured boxes indicate values that meet our defined benchmarking thresholds. All analyses are considered at the resolution of the coarsest CMIP6 GCM (i.e., NESM3, ~ 216km).
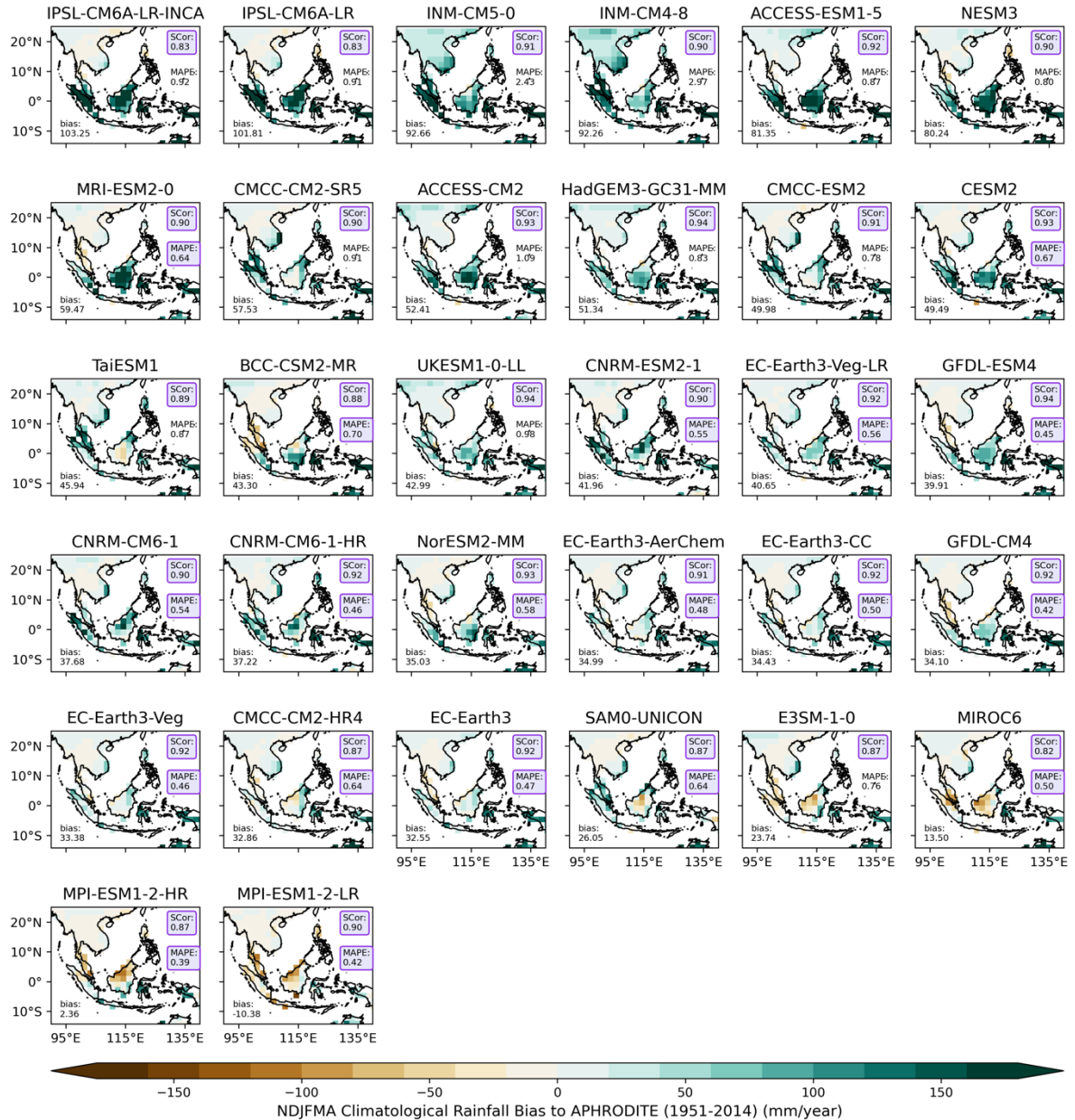
Figure 3. Same as figure 2 but for the dry season (Nov-April; NDJFMA).

The corresponding results for the dry season reveal some interesting features (Fig. 3). First, there are substantial similarities in the spatial distribution of climatological rainfall biases across models during this season. CMIP6 GCMs consistently show small biases over Indochina and large wet biases over MC. A better spatial correlation with observations (i.e., Scor > 0.8) is obtained during the dry season, consistent with previous findings [e.g., CORDEX-CMIP5 RCMs (Nguyen et al., 2022) or CMIP6 GCMs (Desmet and Ngo-Duc, 2022)] in highlighting the dependence of model performance on the season. With improved performance in capturing the spatial variation of total precipitation intensity compared to the wet season, all models meet our expected performance in spatial variability. However, INM- and IPSL-family models still fail the MAPE criterion since they exhibit much higher precipitation intensity than APHRODITE, particularly over MC. Note that over SEA, APHRODITE is drier than other precipitation products particularly over MC (Nguyen et al., 2020).

341 It is important to note that whether a model passes or fails the benchmarking is strongly dependent on the choice
342 of threshold as emphasised in Isphording et al. (2024). For instance, more simulations would fail this test if we
343 set a higher threshold of Scor, notably for the MJJASO season case.

3.1.2. Seasonal cycle

345 In this section, we follow the simplified method developed by Isphording et al. (2024) in quantifying the phase
346 and structure of the seasonal cycle. In particular, we rank total monthly precipitation from wettest to driest. We
347 then define the benchmarking threshold such that the four wettest and driest observed months must fall within the
348 six wettest and driest months simulated by models (Fig. 4).
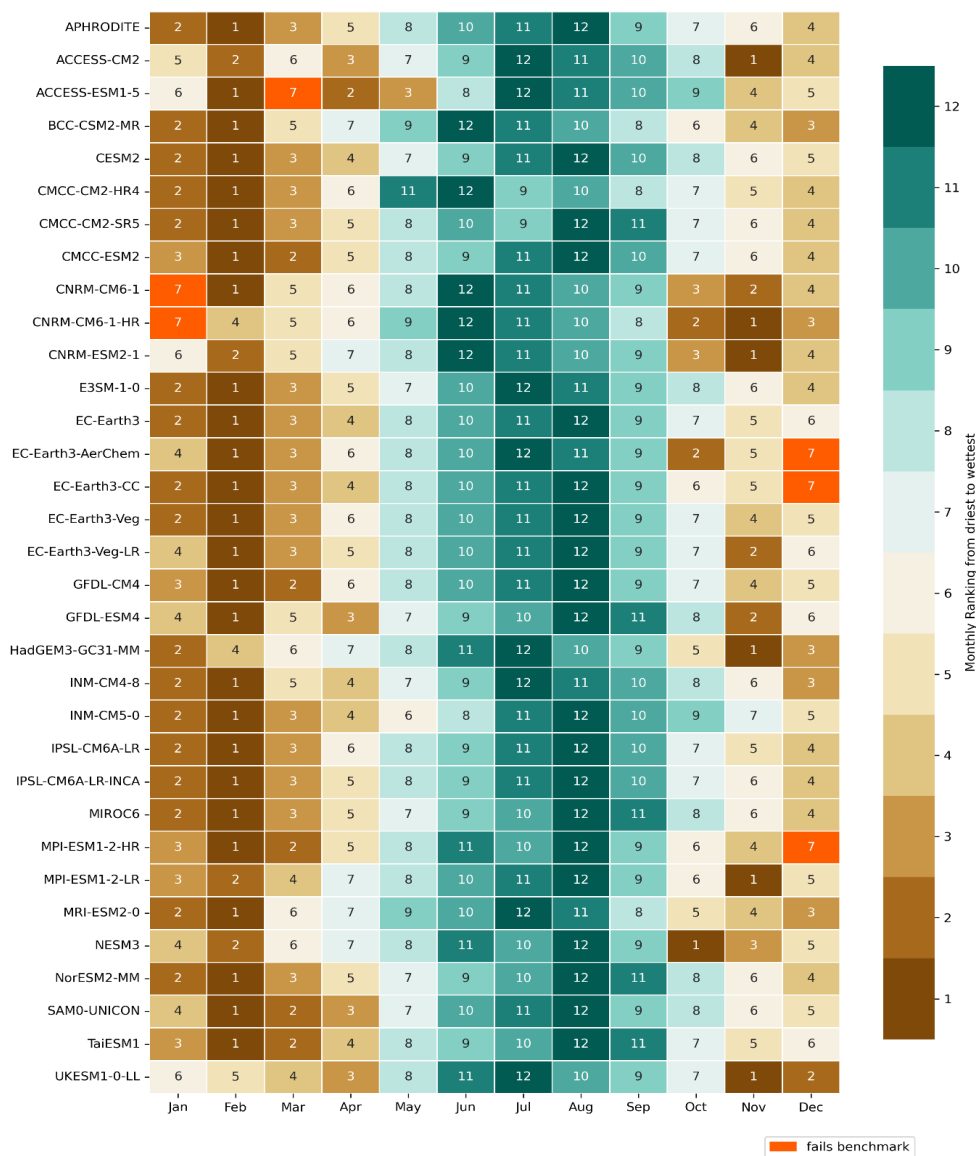
Figure 4. The climatological (1951-2014), average total monthly rainfall over the mainland Southeast Asia are ranked from driest to wettest for each CMIP6 simulation. Brown shades (1-6) indicate the six driest months while teal colours (7-12) indicate the six wettest months. The models failed in benchmarking are highlighted in orange colour. All analyses are considered at the coarsest CMIP6 GCM (i.e., NESM3, ~ 216km).

Overall, most CMIP6 GCMs reproduce the phase well but tend to overestimate precipitation intensity, notably for the observed precipitation peaks during boreal summer (Fig. s3). The INM- and IPSL-family simulations stand out, consistent with the wettest biases observed in spatial patterns (section 3.1.1).

According to the benchmarking threshold definitions, all models meet the benchmark for simulating the four wettest observed months. However, six models do not pass the benchmark for simulating the four driest observed months, as highlighted in orange in Fig. 4. Specifically, one of the four driest months according to the APHRODITE dataset (December through March) is ranked as the sixth wettest month (ranked 7th in Fig. 4) by these models.

3.1.3. Significant trend

The final MSM aims to explore how rainfall changes over time (Isphording et al., 2024). In this part, we compare the signal of statistically significant simulated and observed trends using the wet (Fig. 5) and dry (Fig. 6) seasons accumulated precipitation. A Theil-Sen trend is calculated over a 65-year period (1951-2014) and tested at a 5% significance level using a Mann-Kendall significant test (Kendall, 1975).

There is a significant decreasing trend in observed total precipitation during the wet season (Figure 5 – top panel) while the dry season has a significant increasing trend (Figure 6 - top panel). A model fails this benchmark if it exhibits an opposite significant trend to that of the observations. Using this definition, all models pass this benchmark during the wet season, but MRI-ESM2-0 and MPI-ESM-1-2-HR fail during the dry season.

Note that AR6 [Chapter 8 (Douville et al., 2021)] stated much more confidence in precipitation trends over MC after 1980. Therefore, we conducted an additional trend calculation (figures not shown) over the 33-year (1982-2014) period for all considered observational products. Although there are differences in the slope of changes among observational products, their direction (not shown) remains the same as the 1951-2014 period.

375
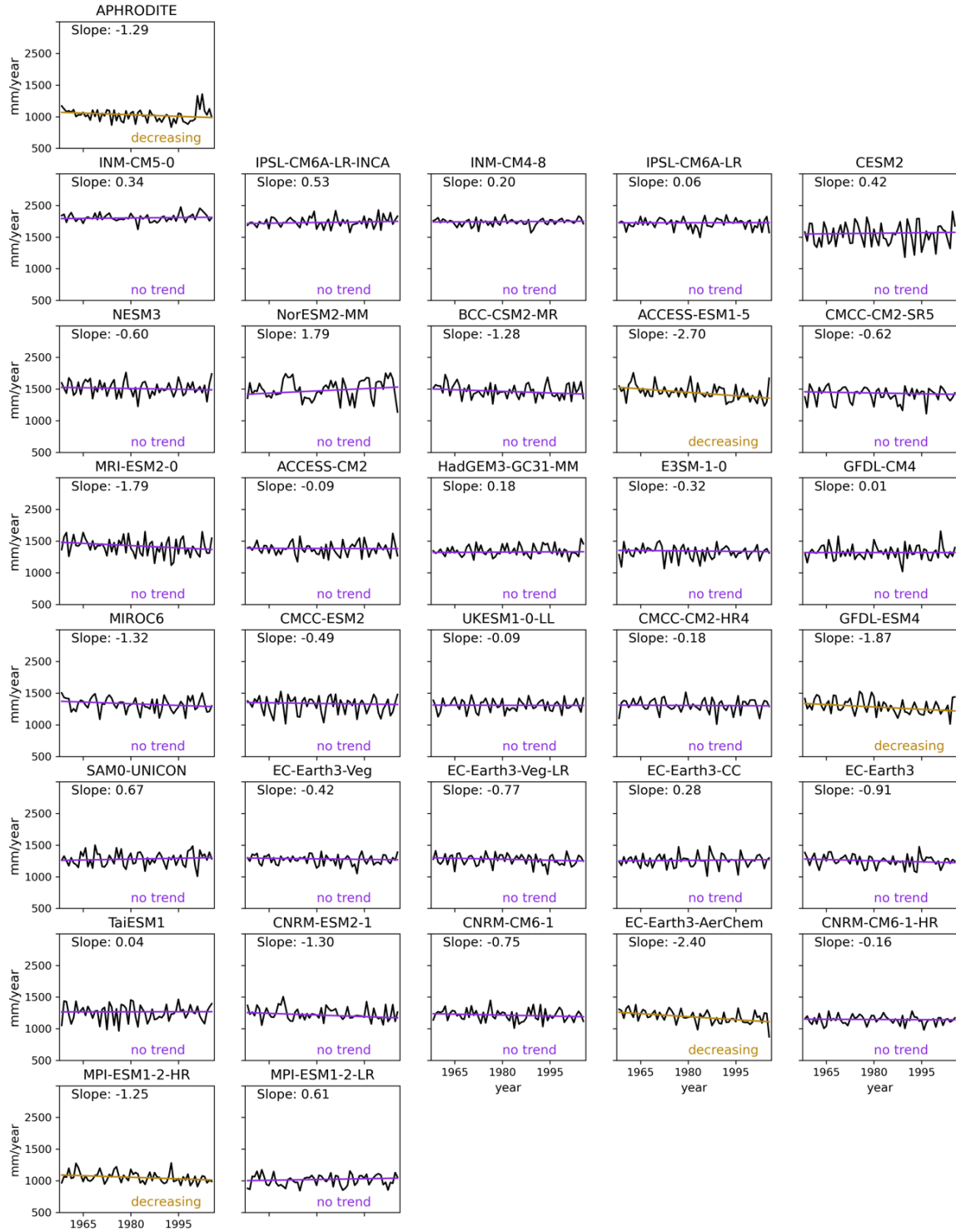
Figure 5. The observed (top row) and modelled seasonal average total precipitation across Southeast Asia land areas during the wet season (May-October, MJJASO) for the period 1951-2014. The direction of the observed Thiel-Sen trend is the benchmark (top row). The Thiel-Sen trend line for each of the simulations is plotted in grey if the models fail the benchmark and in purple if they pass. The magnitude of the trend is noted in the top middle corner and the results of the Mann-Kendall significance test is noted in the bottom right corner. Models are sorted based on the magnitude of the spatial average to match the order of Figure 2. All analyses are considered at the coarsest CMIP6 GCM (i.e., NESM3, ~ 216km). All models pass the benchmark.

383
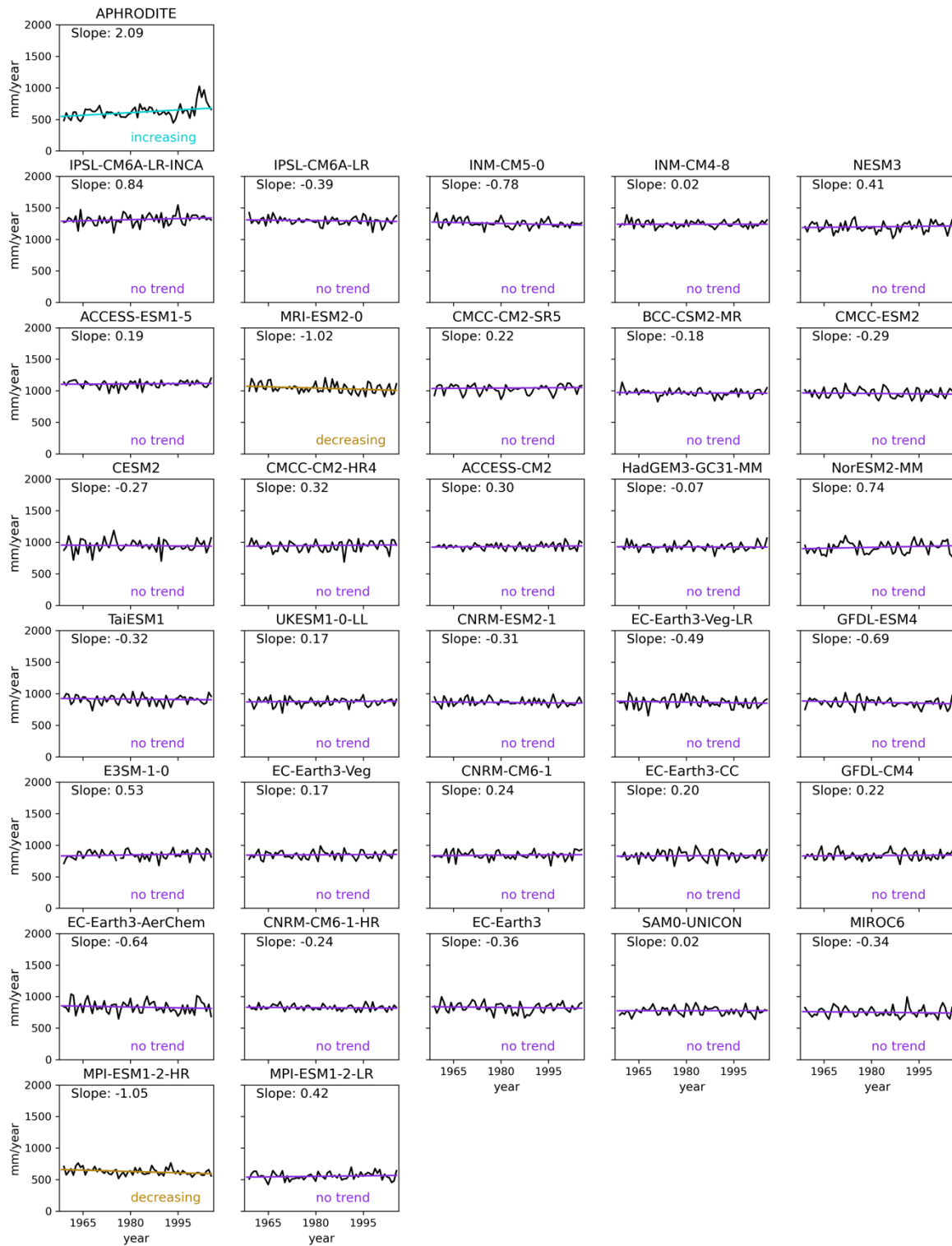
384

385 **Figure 6.** Same as Figure 5 but for the boreal dry season (November – April, NDJFMA).

386 Table 3 summarizes the MSM benchmarking results for the 32 CMIP6 GCMs tested. There are 19 simulations

387 that pass all MSMs and therefore meet the minimum requirements for the purpose of this study.

Table 3. Summary of model performance against the MSMs for precipitation. Models pass the benchmarks are highlighted in **bold.**

Simulations	Wet season		Dry season		Seasonal cycle	Trend		Pass/7
	MAPE	Scor	MAPE	Scor		Wet	Dry	
ACCESS-CM2	+	+	+	+	+	+	+	**7**
ACCESS-ESM1-5	+	+	+	+	-	+	+	6
BCC-CSM2-MR	+	+	+	+	+	+	+	**7**
CESM2	+	+	+	+	+	+	+	**7**
CMCC-CM2-HR4	+	+	+	+	+	+	+	**7**
CMCC-CM2-SR5	+	+	+	+	+	+	+	**7**
CMCC-ESM2	+	+	+	+	+	+	+	**7**
CNRM-CM6-1	+	+	+	+	-	+	+	6
CNRM-CM6-1-HR	+	+	+	+	-	+	+	6
CNRM-ESM2-1	+	+	+	+	+	+	+	**7**
E3SM-1-0	+	+	+	+	+	+	+	**7**
EC-Earth3-AerChem	+	+	+	+	-	+	+	6
EC-Earth3-CC	+	+	+	+	-	+	+	6
EC-Earth3	+	+	+	+	+	+	+	**7**
EC-Earth3-Veg	+	+	+	+	+	+	+	**7**
EC-Earth3-Veg-LR	+	+	+	+	+	+	+	**7**
GFDL-CM4	+	+	+	+	+	+	+	**7**
GFDL-ESM4	+	+	+	+	+	+	+	**7**
HadGEM3-GC31-MM	+	+	+	+	+	+	+	**7**
INM-CM4-8	-	+	-	+	+	+	+	5
INM-CM5-0	-	+	-	+	+	+	+	5
IPSL-CM6A-LR	-	-	-	+	+	+	+	4
IPSL-CM6A-LR-INCA	-	-	-	+	+	+	+	4
MIROC6	+	+	+	+	+	+	+	**7**
MPI-ESM1-2-HR	+	+	+	+	-	+	-	5
MPI-ESM1-2-LR	+	+	+	+	+	+	+	**7**
MRI-ESM2-0	+	-	+	+	+	+	+	6
NESM3	+	+	-	+	+	+	+	5
NorESM2-MM	-	+	+	+	+	+	+	6
SAM0-UNICON	+	+	+	+	+	+	+	**7**
TaiESM1	+	+	+	+	+	+	+	**7**

While the BMF was designed for precipitation, we can also apply the MSMs to other climate variables such as annual mean near-surface temperature (see Supplementary Fig. s4-7 and Tables s1). For temperature, we use the APHRODITE daily temperature datasets [version V1204R1 and V1204XR (Yatagai et al., 2012)] that span 1961–2015. In general, CMIP6 GCMs show biases for average temperature, with a greater number of GCMs exhibiting cold biases rather than warm biases (Fig. s4). Almost all models succeed in simulating the observed spatial

distribution (e.g., Scor greater than 0.75), phases (e.g., no model fails the benchmarking for temperature annual cycle, Figures s5-6) and historical trends (e.g., increase trend, Fig. s7) of temperature. Overall, models are better at simulating temperature characteristics (e.g., spatial pattern, annual cycle, and trend) than precipitation over SEA. Out of four models that fail the MSMs for near-surface temperature, two INM-family simulations do not meet the expected spatial distribution benchmark (Scor ≥0.85) while CNRM-CM6-1-HR and NESM3 show the largest relative errors compared to APHRODITE (MAPE = 0.08). These four models also fail in MSMs for precipitation, as discussed above.

3.2 Versatility metrics – Process-oriented metrics

In addition to the MSMs, our aim is to select a subset of GCMs for dynamical downscaling that simulate precipitation mechanisms. Therefore, in the next steps we focus on process-oriented metrics which capture the relationship between precipitation and other variables well.

3.2.1. Monsoon wind

We seek to identify models that adequately depict the low-level circulation over SEA during two prominent seasons: boreal summer (June-September; JJAS) and winter (December-February, DJF), by comparing them to ERA5 (Fig. 7 and 8 respectively). To measure the agreement between simulated and observed wind patterns in terms of intensity and direction, we employ three metrics: Scor; MAPE and MD (see section 2.2.3) and we set the benchmarking threshold for each metric in dealing with limited simulations at this versatility stage. In particular, we define the threshold for wind intensity as MAPE ≤ 0.65 to seek models that do not overestimate the amplitude of monsoon wind. In terms of wind structure, we set a stricter benchmarking threshold for Scor as ≥ 0.70, aiming to retain models that adequately represent the distribution of wind intensity across the whole region. Recognizing that wind magnitude might be the same at a location, but different directions could substantially impact rainfall patterns, we consider a threshold for direction MD as ≤ 20 degrees. This criterion helps to eliminate models where high-speed wind direction deviates significantly from observed patterns.

During summer, ERA5 shows westerly winds flowing from the Bay of Bengal into Indochina, then deviating northward to the northern Philippines (along 10N). Concurrently, easterly winds from Australia traverse MC and Papua (see Fig. 7). Conversely, in winter, the wind patterns are largely reversed (Fig. 8). The easterly and north-easterly winds from the north pass through the Philippines, reaching the southern coast of Vietnam and the Malaysian peninsula, while westerly winds predominate between the Indonesian islands towards Papua.

Overall, the subset of CMIP6 GCMs capture the circulation structure relatively well (Scor ranging from 0.72 to 0.92 for DJF and from 0.81 to 0.95 for JJAS) but tend to overestimate the wind intensity relative to ERA5, particularly over high-speed wind areas. For example, the westerly component from the Bay of Bengal during JJAS or the easterly component over MC during DJF is too strong compared to ERA5. These might link with the wet biases discussed in section 5.1. Interestingly, all MSM-selected models for precipitation capture the direction of the main components of JJAS monsoon flow well.

429
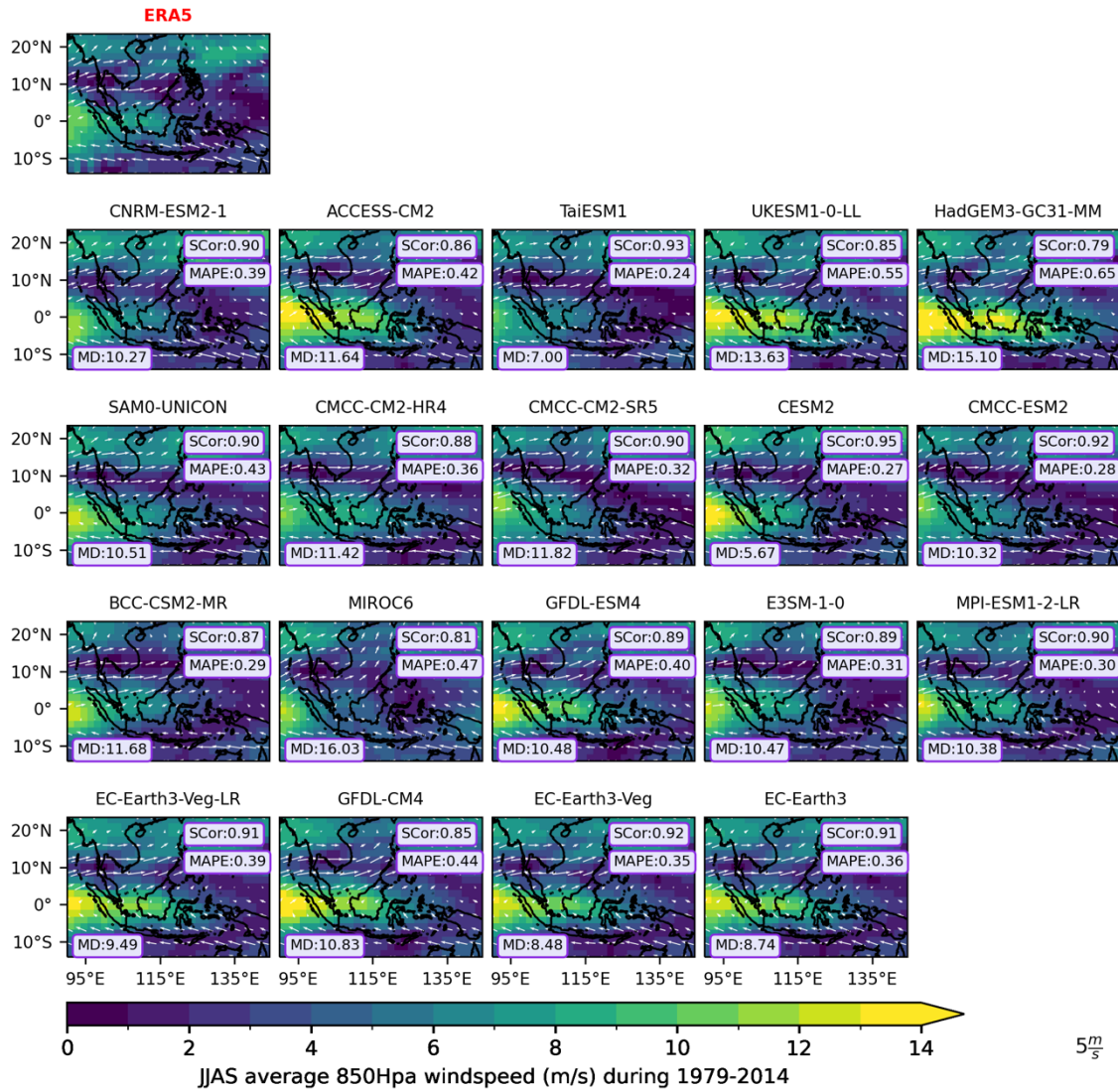
Figure 7. The spatial distribution of the climatology (1979-2014) of low-level wind circulation during the summer (JJAS) (vectors) in ERA5 reanalysis (highlighted by red title) and for individual simulations selected using MSM. All analyses are considered at the coarsest CMIP6 GCM (i.e., NESM3, ~ 216km). Shading indicates the magnitude of wind (in m s^{-1}). The mean absolute percentage error (MAPE) and spatial correlation (Scor) calculated against ERA5 are plotted in the upper right corners respectively. The mean of difference in wind direction (MD) referenced to ERA5 is shown in the lower left corner. Values highlighted in purple-coloured boxes indicate that they meet our defined benchmarking thresholds. Models are ranked from highest to lowest values of MD.
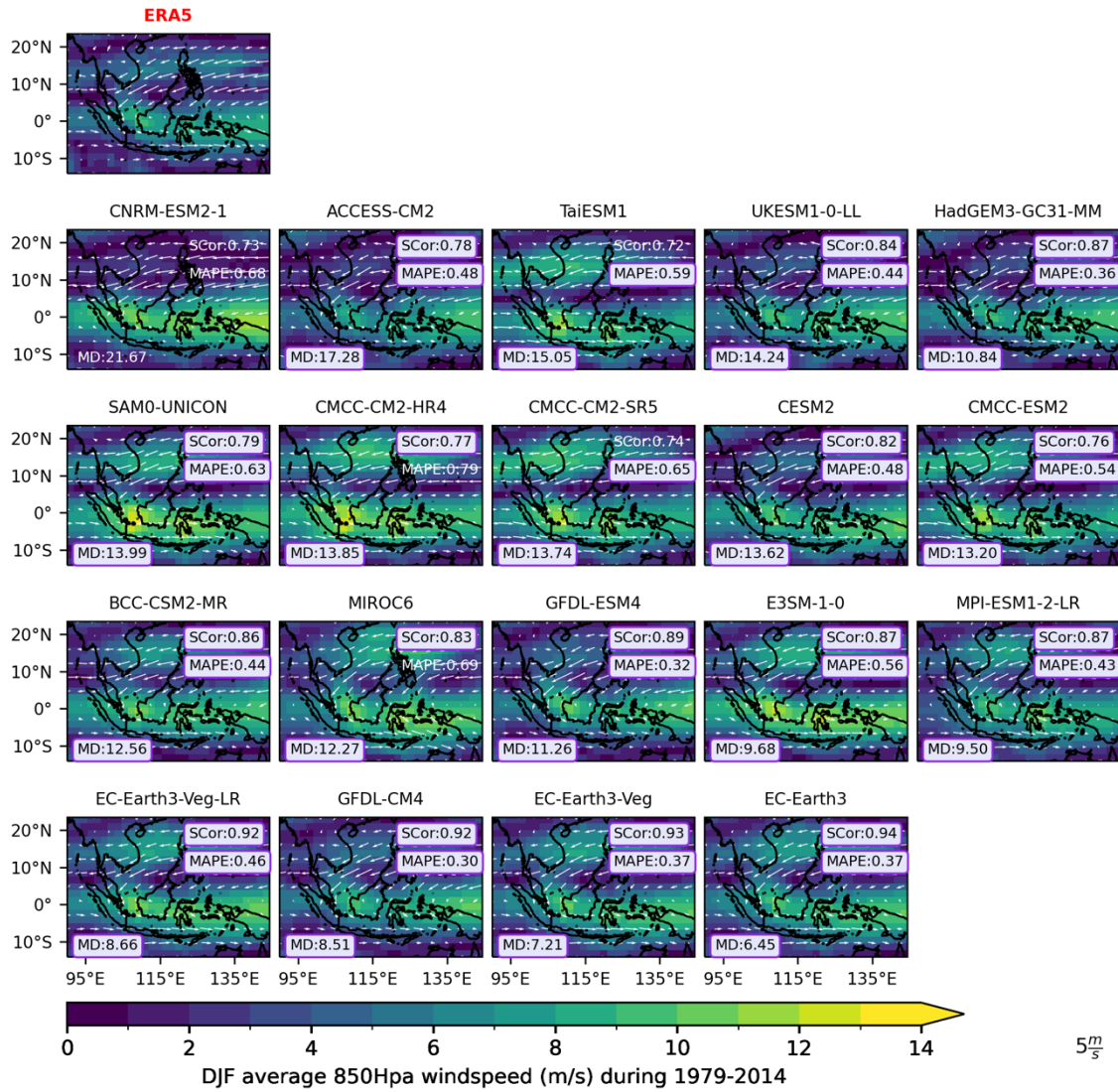
Figure 8. Same as Figure 7 but for the boreal winter wind (December-February, DJF)

Using the definition of benchmark thresholds mentioned above, all models meet our expectations for wind intensity (MAPE) during the summer season but two fail for the winter season (i.e., MAPE of 0.79 for CMCC-CM2-HR4 and 0.69 for MIROC6). Interestingly, only one model fails in benchmarking for wind spatial distribution and direction: CNRM-ESM2-1 (MD is 21.67 during DJF, Fig. 8).

3.2.3 Rainfall teleconnections with modes of variability

The rainfall teleconnection for DJF ENSO is examined for two different seasons: the extended summer season of the developing year (MJJASO of year 0) the boreal spring of the following year (MAM of year +1) while the precipitation-IOD teleconnection is analysed for boreal autumn (SON). To benchmark CMIP6 GCMs, three metrics (HR, MR and FAR, see section 2.2.3) are calculated for each GCM considering the thresholds ≥ 0.5 for HR and ≤ 0.65 for MR and FAR, given the limited number of simulations used at this stage.

Correlation of DJF Nino34 (year 0) and MJJASO (year 0) precipitation anomalies (1951-2014)
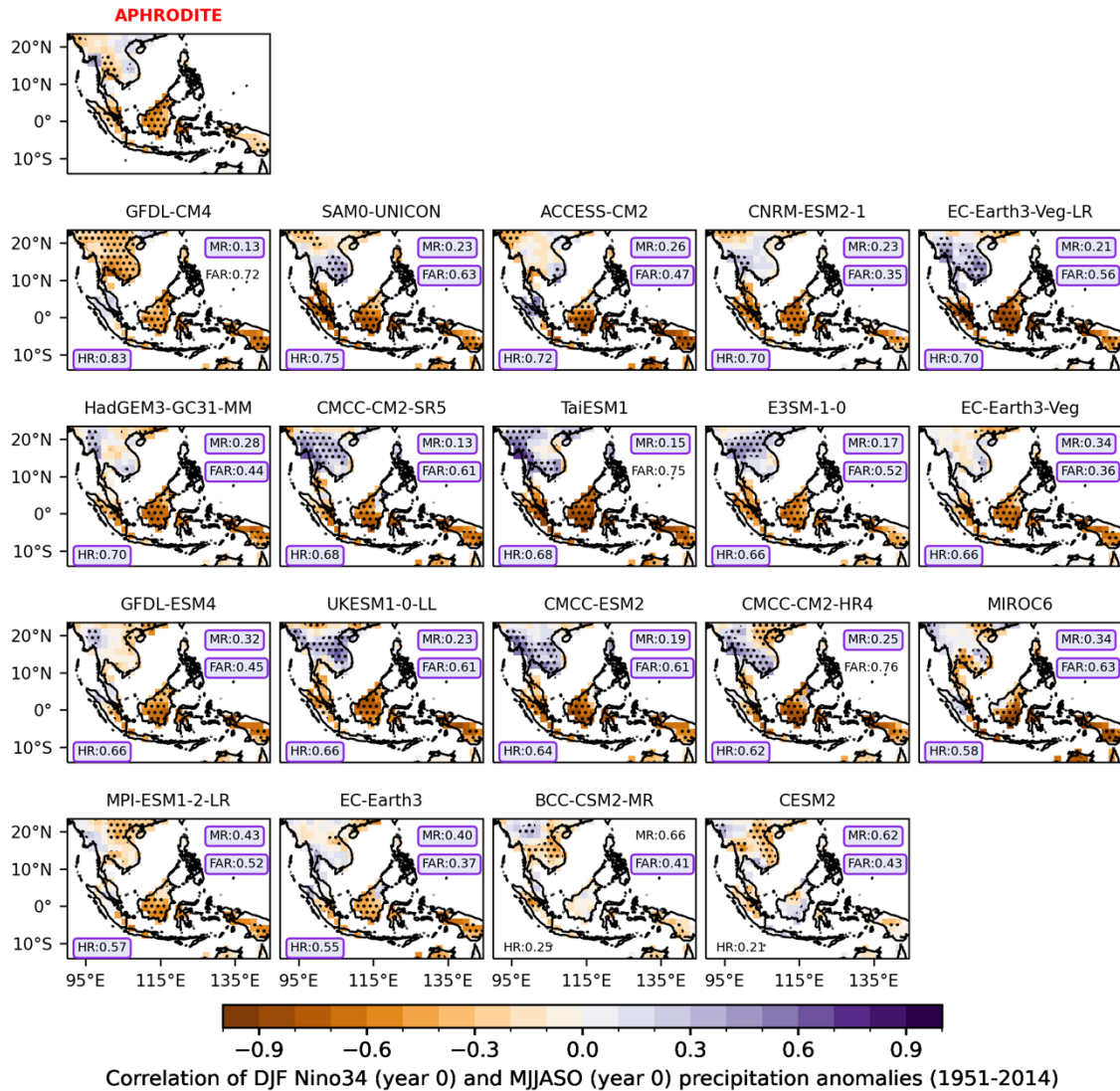
Figure 9. Lead correlation coefficients of the boreal summer (May-October, MJJASO year 0) rainfall with the mature phase of ENSO (December-January-February, DJF year 0 of Niño3.4 indices) for observations from APHRODITE with HadISST; individual CMIP6 GCM models during the period 1951-2014. The stippling indicates the grid points where the correlation coefficient is statistically significant at 95% confidence level according to the Student t-test. The Hite Rate (HR), Miss Rate (MR) and False Alarm Rate (FAR) calculated against APHRODITE are shown in the bottom left and upper right corners respectively. All analyses are considered at the coarsest CMIP6 GCM (i.e., NESM3, ~ 216km). Values highlighted in purple-coloured boxes indicate values that meet our defined benchmarking thresholds. Models are ranked from highest to lowest values of HR.

The results for observations and CMIP6 GCMs selected from MSMs are shown in Fig. 9-11 respectively. The observed teleconnections vary widely by region and season. In general, ENSO-induced summer rainfall variability is dominant over MC (e.g., Sumatra and Java, Fig. 9), while spring variability is dominant over Indochina, northern Borneo and Philippines (Fig. 10), which agrees with the evolution and seasonal circulation migration mentioned in previous literature (Juneng and Tangang, 2005; Supari et al., 2018; Wang et al., 2020). On the other hand, IOD-induced rainfall variability is more pronounced during the SON season over MC (Fig. 11).
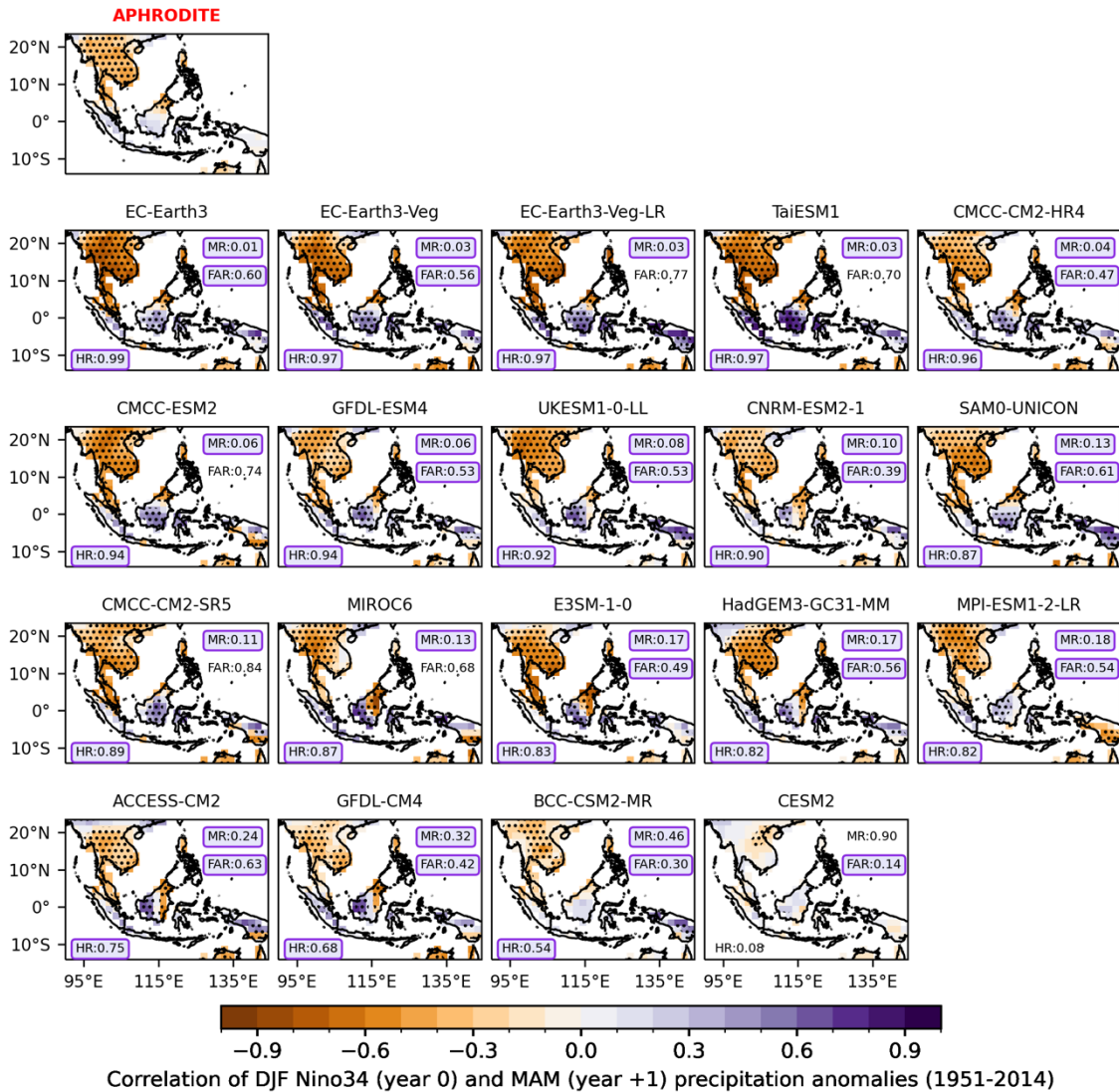
Figure 10. Similar with Figure 9 but for the lag correlation coefficients the mature phase of ENSO (December-January-February, DJF year 0 of Niño3.4 indices) with the boreal spring (March-April-May, MAM year +1) rainfall for (a) observations from APHRODITE with HadISST; (b)-(k) individual CMIP6 GCM models during the period 1951-2014. Models are ranked from highest to lowest values of HR. All analyses are considered at the coarsest CMIP6 GCM (i.e., NESM3, ~ 216km).

CMIP6 GCMs (Fig. 10) demonstrate reasonable accuracy in simulating the spatial distribution of the ENSO teleconnection, but tend to overestimate its strength, particularly over regions where observed temporal correlation coefficients are non-significant. During MJJASO of the developing year, most models successfully reproduce significant negative signals over MC (e.g., high HR values ranging from 0.66 to 0.7 and low MR values less than 0.4). During boreal spring of the following year (MAM of year 1), the ENSO-signals in CMIP6 GCMs match the observed pattern better than those during MJJASO of the developing year (Fig. 9), particularly over Indochina. Higher values of HR and lower MRs are found in most CMIP6 GCMs. This is consistent with previous literature that highlight that GCMs tend to overestimate ENSO variability across much of the equatorial Pacific (Mckenna et al., 2020) produce a poor representation of the ENSO life cycle (Taschetto et al., 2014; Mckenna et al., 2020) and interaction between ENSO and IOD (Mckenna et al., 2020; Planton et al., 2021). Note that certain models consistently perform well across seasons, such as EC-Earth3-Veg, EC-Earth3-CC, GFDL-ESM4 or HadGEM3-GM31-MM while others, like BCC-CSM2-MR and CESM-2, exhibit less favourable performance in capturing

481   ENSO teleconnections over the region (Fig. 9 and 10). Eight out of 19 models, including the EC-Earth3 family,

482   ACCESS-CM2, E3SM1-0, GFDL-ESM4, HadGEM3-GCM31-MM, MPI-ESM1-2-LR, SAM0-UNICON, UK-

483   ESM1-0-LL meet the ENSO teleconnection benchmark. Among models that did not pass the benchmark, many

484   indicate an overestimation of observed non-significant ENSO signals (FAR) over the mainland during the

485   MJJASO of year 0 (e.g., FAR of CMCM-CM2-HR, TaiESM1 andGFDL-CM4 is 0.76, 0.75 and 0.72 respectively)

486   or over MC during MAM of the following year (e.g., FAR of CMCC-CMS-SR5, EC-Earth3-Veg-LR and CMCC-

487   ESM2 are 0.84, 0.77 and 0.74 respectively).

488
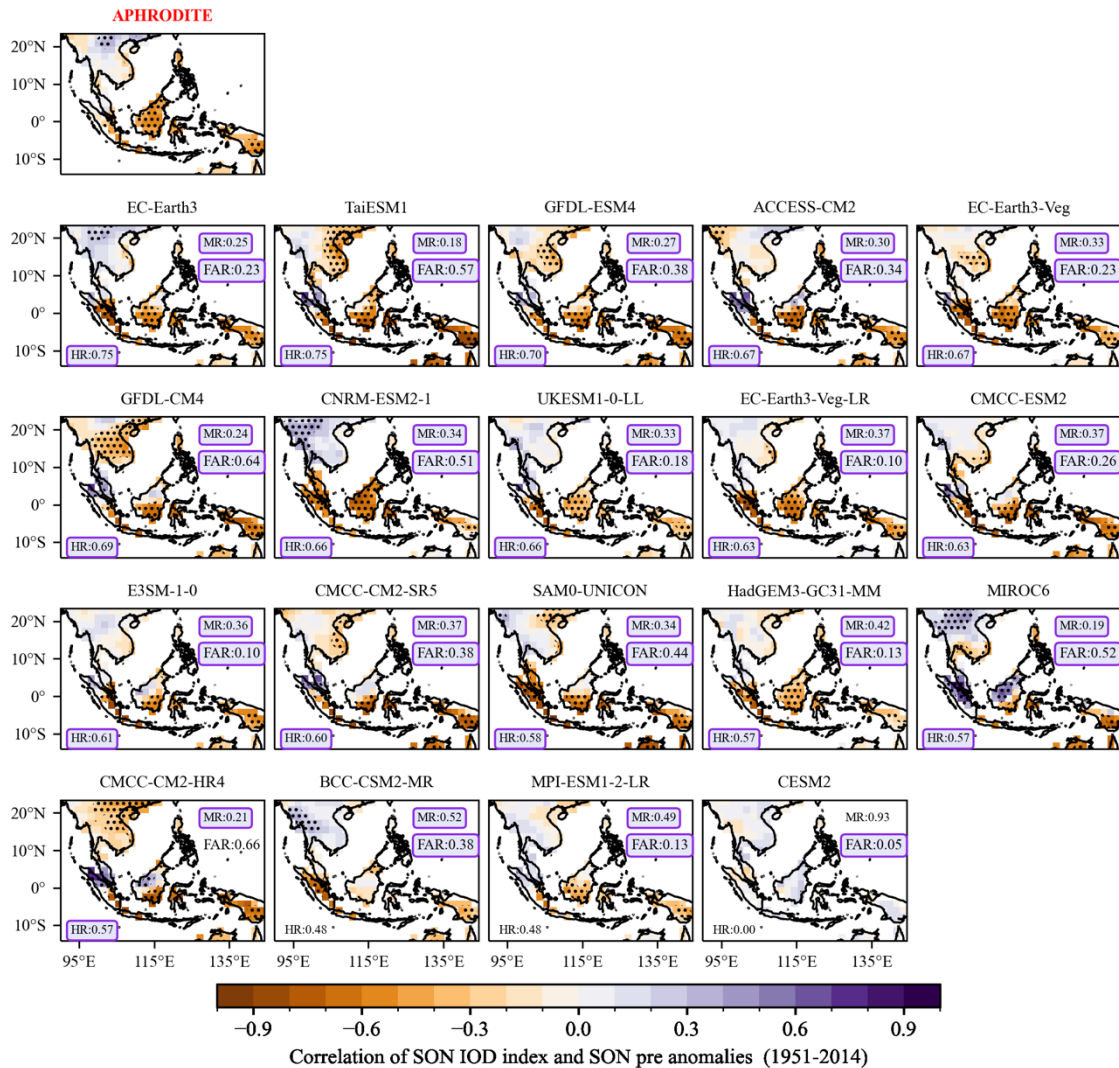
Figure 11. Correlation coefficient of the boreal autumn (September-October-November, SON) rainfall with IOD (DMI)
indices for observations from APHRODITE with HadISST and for individual CMIP6 GCMs during the period 1951-2014.
The stippling indicates the grid points where the correlation coefficient is statistically significant at 95% confidence level
according to the Student t-test. The Hite Rate (HR), Miss Rate (MR) and False Alarm Rate (FAR) calculated against
APHRODITE are plotted in the bottom left and upper right corners respectively. Values highlighted in purple-coloured boxes
indicate values that meet our defined benchmarking thresholds. Models are ranked from highest to lowest values of HR. All
analyses are considered at the coarsest CMIP6 GCM (i.e., NESM3, ~ 216km).

496   Interestingly, the precipitation-IOD teleconnection shows some notable similarities among the 18 CMIP6 GCMs

497   considered at the versatility metrics stage (Fig. 11). Most models capture the significant negative correlation over

498   Java and southern Borneo, resulting in high HR values (ranging from 0.58 to 0.75). An exception is CESM2,

which produces non-significant signals over the entire region (Fig. 11). Interestingly, models that demonstrate weak performance in simulating ENSO teleconnections (e.g., BCC-CSM2-MR, CESM2 and CNCC-CM2-HR) also struggle to accurately simulate the IOD teleconnection. Using the same threshold definitions as established for assessing the ENSO teleconnection, we identify 14 out of 18 models that pass the benchmarking for IOD-teleconnection.

Table 4. Summary model performance against the versatility metrics that focused on precipitation drivers and modes of variability (ENSO and IOD teleconnections). Models that meet or exceed the benchmarks are highlighted in **bold**. All analyses are considered at the coarsest CMIP6 GCM (i.e., NESM3, ~ 216km).

Simulations	Monsoon circulation						ENSO Teleconnection						IOD teleconnection			Pass/15
	JJAS			DJF			MJJASO			MAM			SON			
	Scor	MD	MAPE	Scor	MD	MAPE	MR	FAR	HR	MR	FAR	HR	MR	FAR	HR	
ACCESS-CM2	+	+	+	+	+	+	+	+	+	+	+	+	+	+	+	**15**
BCC-CSM2-MR	+	+	+	+	+	+	-	+	-	+	+	+	+	+	+	13
CESM2	+	+	+	+	+	+	-	+	+	-	-	+	-	-	+	10
CMCC-CM2-HR4	+	+	+	-	+	+	+	+	-	+	+	+	-	+	-	11
CMCC-CM2-SR5	+	+	+	+	+	+	+	+	+	+	+	-	+	+	+	14
CMCC-ESM2	+	+	+	+	+	+	+	+	+	+	+	-	+	+	+	14
CNRM-ESM2-1	+	+	+	-	-	-	+	+	+	+	+	+	+	+	+	12
E3SM-1-0	+	+	+	+	+	+	+	+	+	+	+	+	+	+	+	**15**
EC-Earth3	+	+	+	+	+	+	+	+	+	+	+	+	+	+	+	**15**
EC-Earth3-Veg	+	+	+	+	+	+	+	+	+	+	+	+	+	+	+	**15**
EC-Earth3-Veg-LR	+	+	+	+	+	+	+	+	+	+	+	-	+	+	+	14
GFDL-CM4	+	+	+	+	+	+	+	+	-	+	+	+	+	+	+	14
GFDL-ESM4	+	+	+	+	+	+	+	+	+	+	+	+	+	+	+	**15**
HadGEM3-GC31-MM	+	+	+	+	+	+	+	+	+	+	+	+	+	+	+	**15**
MIROC6	+	+	+	-	+	+	+	+	+	+	+	-	+	+	+	13
MPI-ESM1-2-LR	+	+	+	+	+	+	+	+	+	+	+	+	-	+	+	14
SAM0-UNICON	+	+	+	+	+	+	+	+	+	+	+	+	+	+	+	**15**
TaiESM1	+	+	+	+	+	+	+	+	-	+	+	-	+	+	+	13
UKESM1-0-LL	+	+	+	+	+	+	+	+	+	+	+	+	+	+	+	**15**

Given the large observational uncertainty, particularly in rainfall estimation over the region (Nguyen et al., 2020; Nguyen et al., 2022), we apply the BMF using different reference datasets while maintaining a consistent benchmarking threshold definition. This evaluation identifies a similar list of models meeting the minimum standards of performance (Table s1). However, exceptions are noted, for instance, MPI-ESM1-2-LR fails to meet the MSMs when compared with GPDD_FDD but passes with other references. Similarly, NorESM2-MM exhibits varying performance across different observational products. However, even if these two models are included in the subsequent selection steps, they fail to meet one or more versatility metrics. For instance, MPI-ESM1-2-LR fails the IOD-teleconnection benchmark (Fig. 11 and Table 4) while NorESM2-MM fails on the ENSO-teleconnection benchmark; Fig. s9).

516   It is acknowledged that different SST products vary in capturing the teleconnection. Figure s8 indicates the notable

517   similarities among SST products in capturing the response of precipitation with modes of variability over SEA

518   except for the teleconnection between DJF (year 0) ENSO and MJJASO (year 0) precipitation. However, despite

519   the diversity in SST products, the final selection of models passing the BMF remains the same.

520   Table 4 summarises the results of benchmarking 19 CMIP6 GCMs selected from the MSM for the versatility

521   metrics. At this point of applying the BMF, we find 8 models (ACCESS-CM2, E3SM1-0, EC-Earth3, EC-Earth3-

522   Veg, GFDL-CM4, HadGEM3-GC31-MM, SAM0-UNICON, UKESM1-0-LL) meet our expectations in

523   simulating precipitation drivers and teleconnections with modes of variability. This could be due to the fact that

524   IOD is an ENSO artefact (Dommenget, 2011).

3.3 Future climate change signals and model dependence
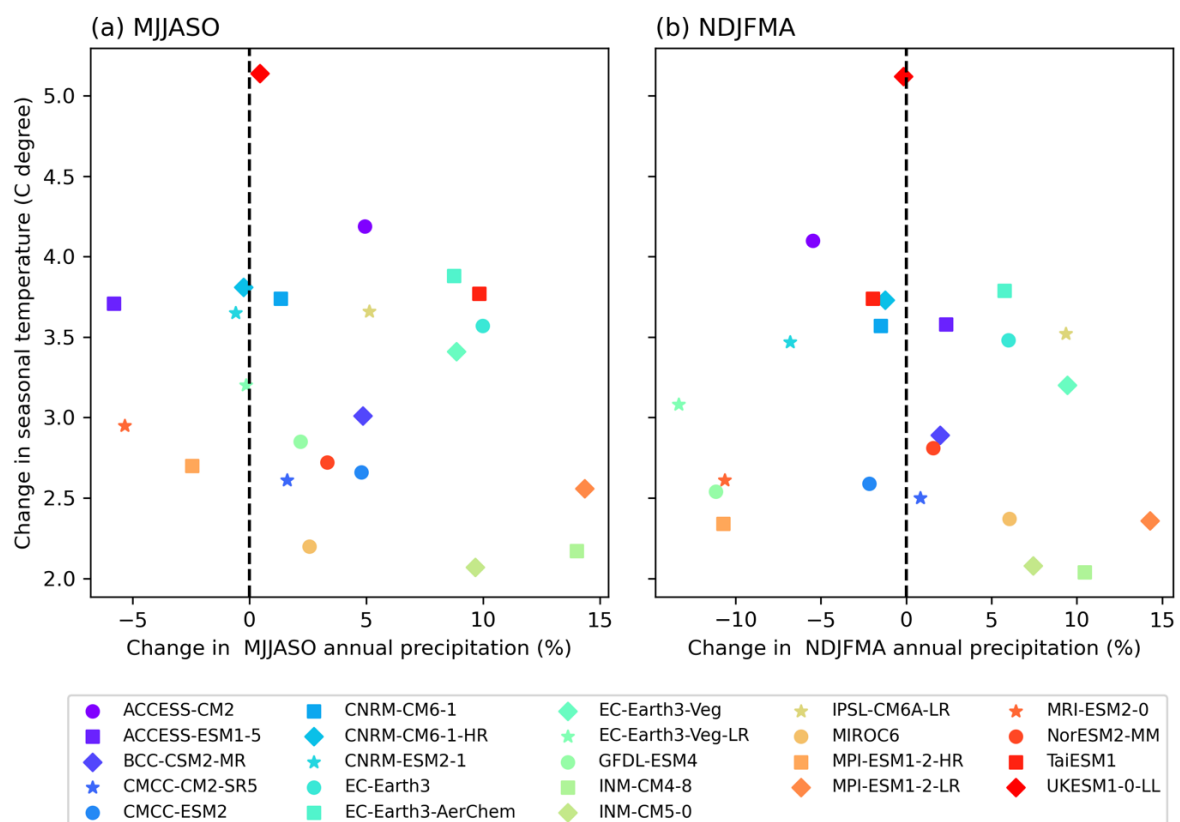
Figure 12. CMIP6 GCM climate change signal (2070-2099 relative to 1961-1990) over mainland Southeast Asia during (a) the wet (MJJASO) and (b) the dry (NDJFMA) seasons. The analyses are conducted for the GCMs that simulated at least monthly near-surface air temperature (tas) and precipitation (pr) for the SSP-3.70 scenario. Note that some models that did not simulate tas or pr for SSP-3.70 (e.g., E3SM1-0, HadGEM3-GCM31-MM, SAM0-UNICON) are not plotted.

531   In this section, we examine the climate change signals from CMIP6 GCMs that provide at least mean temperature

532   and precipitation data for the SSP3-7.0 scenario across two distinct seasons (see Fig. 12). Note that some models,

533   such as CNRM-CM6-1-HR and EC-Earth3-Veg-LR (listed in Table 1), do not offer the sub-daily data (e.g.,

534   atmospheric variables in three dimensions at 6-hour intervals) required for dynamical downscaling at the time of

535   writing. Nevertheless, we include these models in our analysis to gain insights into the future climate change

536   responses of CMIP6 GCMs. Interestingly, while temperature projections show general agreement of an increasing

537   trend (ranging from 2.1°C to 5.1°C), precipitation projections exhibit large variation in both signal and magnitude

(ranging from -4.3% to 12.9%). Therefore, we cannot see the linear relationship between the change in regional total precipitation and temperature. Among the eight models that pass our BMF a priori expectations, there are only five models that provide at least data for monthly near-surface temperature (tas) and precipitation (pre), and they are distributed across the wide range of temperature and precipitation signals over SEA. They include: the wettest models in both seasons with mid-range projected temperatures [e.g. for the MJJASO season: EC-Earth3 (10 % and 3.6 °C) and EC-Earth3_Veg (8.9% and 3.4 °C), Fig. 12a]; a model with the largest increase in temperature: UKESM1-0-LL (e.g., 5.1 °C during the MJJASO season); a model with larger response in precipitation and lower warming: GFDL-ESM4 (e.g., -11.2 % and 2.5 °C during the MJJASO season) and a model with a high-range temperature and mid-range precipitation response: ACCESS-CM2 (e.g., 4.9% and 4.2 °C during the MJJASO season).
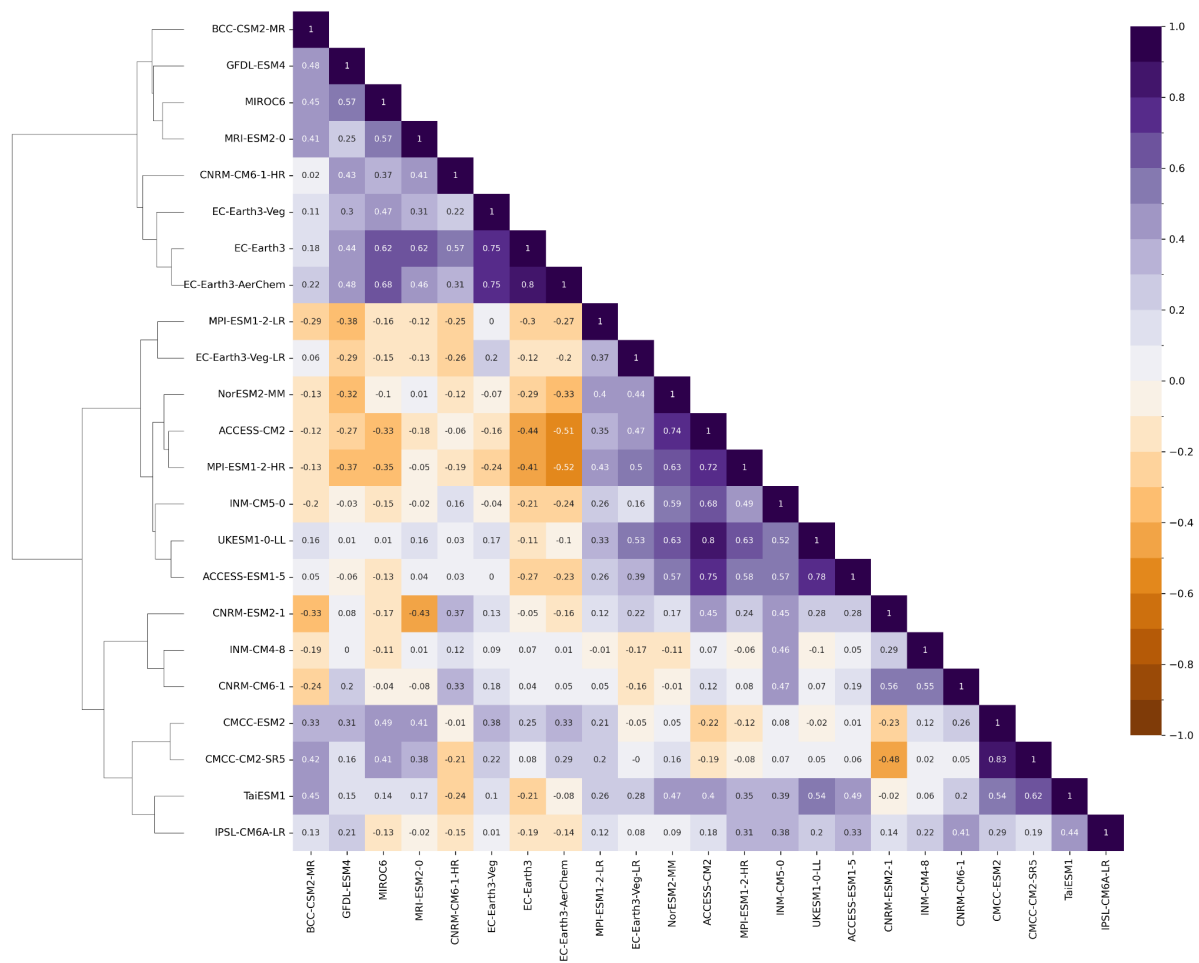
Figure 13. Dendrogram with hierarchical clustering applied for a matrix of spatial correlation coefficient between CMIP6 climate models for the long-term changes (2070-2099 SSP3-7.0 relative to 1961-1990) in total precipitation during the wet season (MJJASO). The matrix is plotted for GCMs that simulated at least monthly near-surface air temperature (tas) and precipitation (pr) for the SSP-3.70 scenario only. Models are clustered with the Ward's linkage criterion.

The dendrogram and matrix of spatial correlation between CMIP6 GCMs are shown for Southeast Asia for climatological bias (Fig. s10-11) and long-term changes (Fig. 13-14) in total precipitation. As before we focus on the wet (MJJASO) and dry (NDJFMA) seasons. Historical correlations highlight notable similarities between models in historical bias maps (mostly significant and greater than 0.5) except UK-ESM1-0-LL which shows poorer relationships with other models (e.g., correlation coefficients with other models are less than 0.5) (Fig s10-

558 11). However, there is higher independence in projection maps compared with that in historical maps. This
559 interesting feature needs to further investigate.

560 Clustering analysis indicates three main spatial change clusters for the MJJASO season, as shown in the
561 dendrogram (Fig. 13). This indicates similarities in the spatial pattern of the climate change response maps (e.g.,
562 correlations greater than 0.5) not only among models from the same families [e.g., among the MetOffice GCM-
563 based family (i.e., UKESM1-0-LL, ACCESS's family] and in model families that share the same model
564 components (e.g., UK-ESM1-0-LL and EC-Earth3 families share the same ocean model of NEMO3.6; Table 1)
565 but also in less obvious families like CNRM and INM families or EC-Earth-based and GFDL-based simulations.
566 An exception is EC-Earth-Veg-LR which appears in different main clusters compared with other EC-Earth-based
567 simulations. As indicated in the MJJASO dendrogram, the BMF-passing models that have data available for
568 dynamical downscaling are in two main clusters including: EC-Earth3/ EC-Earth-veg/ GFDL-ESM4 and
569 UKESM1-0-LL/ ACCESS-CM2.
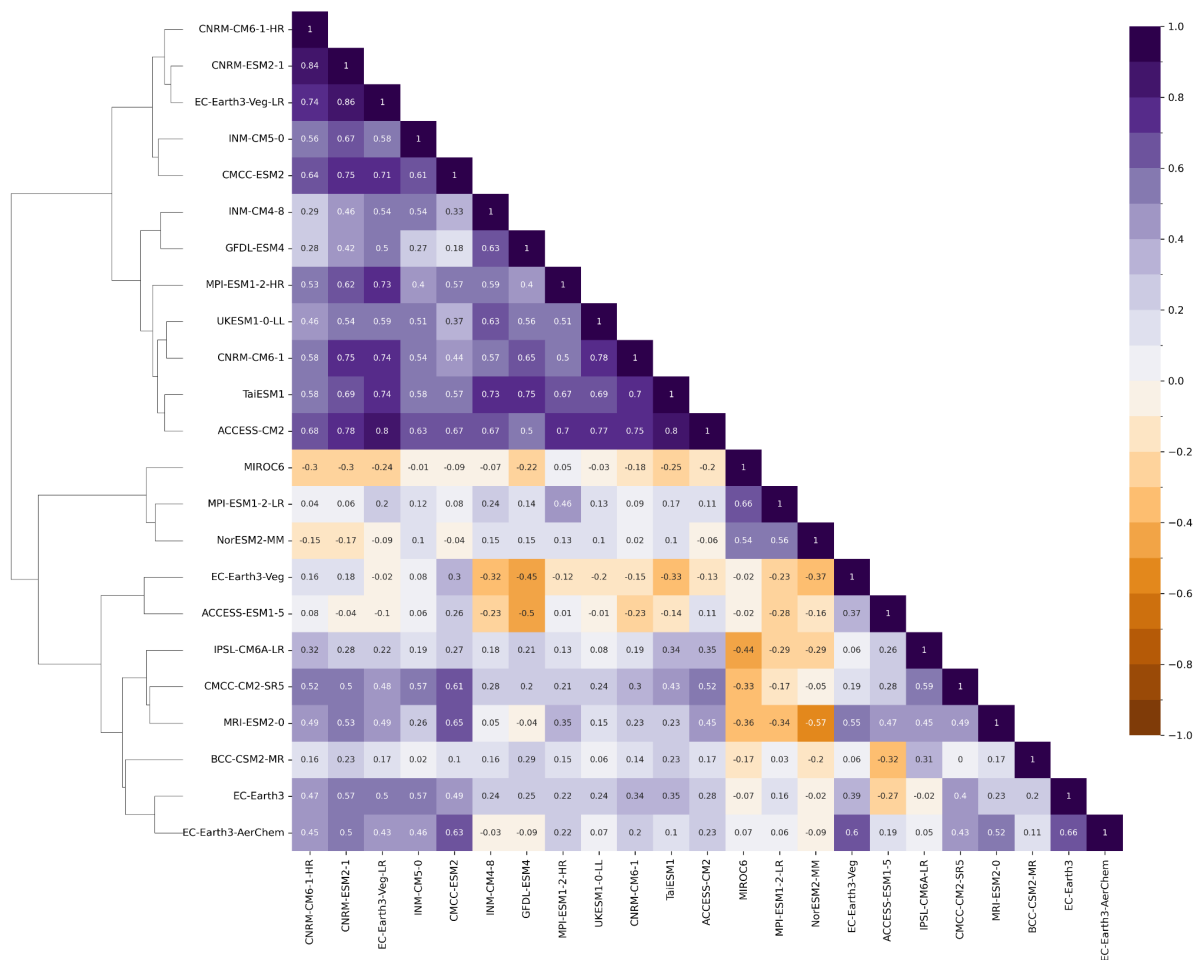
570
571 **Figure 14.** Similar to figure 13 but for the dry season (November – April, NDJFMA).

572 Figure 14 indicates two main spatial change clusters in the dry season. Interestingly, some models from the same
573 family (e.g., EC-Earth3 and EC-Earth-Veg) still belong to the same main cluster but span different branches of
574 the dendrogram. This might be related to the different role of internal variability in determining the level of
575 uncertainty for precipitation during different seasons and needs further investigation. Interestingly, among models
576 that pass the BMF, EC-Earth3 and EC-Earth-veg appear on a main cluster while UKESM1-0-LL, ACCESS-CM2

577   and GFDL-ESM4 are in the other main cluster for the NDJFMA dendrogram. This highlights the dependence of
578   clustering analysis on the season.

579   We acknowledge that a model's good performance in simulating historical climate conditions does not necessarily
580   guarantee similar accuracy in future climate projections, a well-recognized issue in climate modelling (Herger et
581   al., 2019). However, there are no arguments in the literature suggesting that models with weaker skill in simulating
582   historical climatology perform better in future projections. On the contrary, we believe that models demonstrating
583   good performance in both statistical and process-based metrics are more likely to provide credible future
584   projections given their proven ability to accurately simulate the physical mechanisms responsible for generating
585   rainfall in the region.

586   In general, based on our evaluation of model performance, model dependence and future climate change spread,
587   we identify two independent groups of models to use for dynamical downscaling over SEA, that is, EC-Earth3/
588   EC-Earth-Veg, ACCESS-CM2/UKESM1-0-LL. Models from these two groups also offer atmospheric variables
589   in three dimensions at 6-hour intervals required for dynamical downscaling (Table 1). Given the inconsistency of
590   classification of GFDL-ESM4 during different seasons and metrics, it is suggested to consider GFDL-ESM4 with
591   caution.

592   **4 Discussion**

593   Our results somewhat differ from traditional model evaluation studies like Desmet and Ngo-Duc (2022), which
594   ranks models by evaluation metrics and identifies a list of the best models including EC-Earth3, EC-Earth3-Veg,
595   CNRM-CM6-1-HR, FGOALS-f3-L, HadGEM3-GC31-MM, GISS-E2-1-G, GFDL-ESM4, CIESM-WACCM
596   and FIO-ESM-2-0. First, rather than ranking models, our aim is to retain models that meet our predefined
597   expectations (e.g., benchmarking thresholds). Second, the list of examined models is different since we especially
598   focus on models with a resolution greater than 2 degrees to avoid the impacts of coarser resolutions in GCMs on
599   dynamical downscaling. Furthermore, while Desmet and Ngo-Duc (2022) combine model performance in
600   simulating surface climates (e.g., precipitation, near-surface temperature) and climate processes (e.g., low-level
601   atmospheric circulation), our focus is solely on precipitation, its drivers and teleconnections with modes of
602   variability.

603   We acknowledge that the list of models passing the BMF might change, depending on how the benchmarking
604   thresholds are defined. Isphording et al. (2024) notes that the definition of the benchmarking thresholds for the
605   MSMs and versatility metrics can be subjective, and they should be chosen to fit the purpose of the study while
606   incorporating strong scientific reasoning. The strategy employed here involves defining the benchmarking
607   thresholds based on our knowledge of observational uncertainty over the region. In addition, we aim to give each
608   model the 'benefit of doubt', thus retaining a broad range of plausible future climate change responses. In
609   particular, in the initial step of the BMF framework, we are generous in defining the benchmark threshold for the
610   wet season given the lower model performance compared with the dry season. This approach results in 19 out of
611   32 models passing the MSMs. Subsequently we employ versatility metrics to cover a more process-based
612   assessment. Given previous studies have highlighted the overestimation of GCMs in simulating precipitation
613   drivers and its teleconnections and limited possible simulations at this stage, we also set relaxed thresholds for

various metrics to maximize the number of models passing the BMF. We feel this is a pragmatic approach to retain a reasonable sample size and explore plausible futures. However, we acknowledge that dynamical downscaling experiments often require significant computing resources and only a small subset of GCMs should be pre-selected. Therefore, we narrow down our selection of 8 GCMs for further assessment using metrics related to model dependency and future climate change spread.

Previous studies suggest the potential impact of smoothing the extreme values when interpolating to coarser resolutions, which might affect the skill score metrics used to measure percentage errors in a simulation relative to a reference (i.e., MAPE). Although we observe a higher number of failed models for the same skill when conducting the BMF at the GCM original resolutions (Table s4), we identify a similar subset of models meeting all minimum performance requirements (Table s4). This suggests that the coarser resolution of ~210 km used for benchmarking is not the main reason behind the results of quantifying model skill used in this study. This is in line with Nguyen et al. (2022), where they demonstrate that model components (e.g., configurations in different schemes) are the main reason behind the model biases rather than model resolution.

The relationship between model structures and model biases is investigated in the model dependency section using cluster analysis. We acknowledge that grouping of models might changes for not only for considered periods and seasons (as discussed in section 3.3) but also for considered metrics. Interestingly, using mean percentage changes as distance measure between models, we identify similar main clusters of EC-Earth3/ EC-Earth-Veg and ACCESS-CM2/ UKESM1-0-LL among models that passing the BMF (Fig. s12-s13). This subset of models is suitable for dynamical downscaling over Southeast Asia.

The customized BMF implemented in this study offers a consistent framework for model evaluation across the whole CORDEX-SEA domain. The framework can be further developed and applied extensively to sub-regions of interest, in particular within the upcoming Climatic hazard Assessment to enhance Resilience against climate Extremes for Southeast Asian megacities (CARE for SEA megacities) Project of CORDEX-SEA. In this project, each mega city can identify their climate priority and the associated metrics for selecting a fit-for-purpose subset of models. This framework could also be implemented in impact-related projections over SEA, for particular sectors: agriculture, forestry, water etc. for credible future projections.

5 Conclusion

In this paper, we apply the insight gained from the CMIP6 selection process for dynamical downscaling across various CORDEX-domains to Southeast Asia by encompassing several critical factors: model performance, model independence, data availability and the spread of future climate change projections.

Rather than exhaustively evaluating all performance aspects of the models in simulating the Southeast Asian climate, our focus is on selecting models that simulate precipitation well, including its drivers and teleconnections given the high uncertainty in rainfall projections over the region. In addition, we apply a novel standardised benchmarking framework – a new approach in identifying a subset of fit-for-purpose models that align with a user's a priori performance expectations. This framework has two stages of assessment: statistical-based metrics and process/regime-based metrics, conducted for both wet (MJJASO) and dry (NDJFMA) seasons.

From the first step we identify 19 GCMs that meet our minimum criteria for simulating the fundamental characteristics (e.g., bias, spatial distribution, seasonality, and trends) of seasonal rainfall. GCMs generally exhibit wet biases, particularly over the complex terrain of the Maritime Continent. These models then undergo a second evaluation, focusing on their ability to simulate climate processes and teleconnections with modes of variability. While these models consistently capture atmospheric circulation and teleconnections with modes of variability over the region, they exhibit a tendency to overestimate their strength. Ultimately, our framework narrows down the selection to eight GCMs that meet our model performance expectations in simulating fundamental characteristics of precipitation, key drivers, and teleconnections over Southeast Asia. There are obvious high-performing GCMs from allied modelling groups, highlighting the dependency of the subset of models identified from the framework. Consequently, additional tests on model independence, data availability for the SSP 3-7.0, and the spread of future climate change are conducted. These tests lead to the identification of two independent groups of models (e.g., EC-Earth3-Veg/EC-Earth3 and ACCESS-CM2/UKESM1-0-LL) that align with our a priori expectations for dynamical downscaling over CORDEX-SEA. It is recommended that only one model from each group be chosen to avoid models that are too closely related.

Code availability

Codes for benchmarking the CMIP6 GCMs performance (Isphording, 2024) are available from https://doi.org/10.5281/zenodo.8365065

Data availability

Data used in this study is available through:

CMIP6 GCMS at the Earth System Grid Federation (ESGF):

 https://esgf.nci.org.au/projects/esgf-nci/.

ERA5 (Hersbach et al. 2020): https://doi.org/10.24381/cds.bd0915c6.

OISST version 2.1 (Huang et al. 2021):

https://www.psl.noaa.gov/data/gridded/data.noaa.oisst.v2.highres.html.

ERSST version 5 (Huang et al. 2017):

https://www.ncei.noaa.gov/pub/data/cmb/ersst/v5/netcdf/.

APHRODITE version V1101R1 and V1101 XR (Yatagai et al., 2012):

https://www.chikyu.ac.jp/precip/english/index.html.

Author contributions

RNI built the BMF used in this research. PLN applied and developed the BMF for the region of interest, performed the analysis and prepared the original manuscript. LVA, MJT, SCHN and JLM supervised the research, reviewed and edited the manuscript.

Declaration of Competing Interests

The authors declare that they have no known competing financial interests or personal relationships that could have appeared to influence.

Acknowledgements

This work was supported by the Australian Research Council (ARC) Grant FT210100459. LVA and RNI are also supported by ARC grant CE17010023. RNI is also supported by a Scientia PhD scholarship from UNSW. The research was undertaken with the assistance of resources and services from the National Computational Infrastructure (NCI), which is supported by the Australian Government. The codes and graphics visualization for the assessment of CMIP6 GCMs based on the benchmarking framework suggested in Isphording et al. (2024) and Isphording (2024).

References

Abramowitz, G.: Towards a benchmark for land surface models, Geophysical Research Letters, 32,
695 https://doi.org/10.1029/2005GL024419, 2005.

Abramowitz, G.: Towards a public, standardized, diagnostic benchmarking system for land surface models, Geosci. Model Dev., 5, 819-827, 10.5194/gmd-5-819-2012, 2012.

Alexander, L. V., Bador, M., Roca, R., Contractor, S., Donat, M. G., and Nguyen, P. L.: Intercomparison of annual precipitation indices and extremes over global land areas from in situ, space-based and reanalysis products, Environmental Research Letters, 700 15, https://doi.org/10.1088/1748-9326/ab79e2, 2020.

Allan, R., Chambers, D., Drosdowsky, W., Hendon, H., Latif, M., Nicholls, N., Smith, I., Stone, R., and Tourre, Y.: Is there an Indian Ocean dipole and is it independent of the El Niño-Southern Oscillation, CLIVAR exchanges, 21, 18-22, 2001.

Amirudin, A. A., Salimun, E., Tangang, F., Juneng, L., and Zuhairi, M.: Differential influences of teleconnections from the Indian and Pacific Oceans on rainfall variability in Southeast Asia, Atmosphere, 11, 886, 2020.

705 Andrews, M. B., Ridley, J. K., Wood, R. A., Andrews, T., Blockley, E. W., Booth, B., Burke, E., Dittus, A. J., Florek, P., Gray, L. J., Haddad, S., Hardiman, S. C., Hermanson, L., Hodson, D., Hogan, E., Jones, G. S., Knight, J. R., Kuhlbrodt, T., Misios, S., Mizielinski, M. S., Ringer, M. A., Robson, J., and Sutton, R. T.: Historical Simulations With HadGEM3-GC3.1 for CMIP6, Journal of Advances in Modeling Earth Systems, 12, e2019MS001995, https://doi.org/10.1029/2019MS001995, 2020.

710 Baquero-Bernal, A., Latif, M., and Legutke, S.: On dipolelike variability of sea surface temperature in the tropical Indian Ocean, Journal of Climate, 15, 1358-1368, 2002.

Best, M. J.: The plumbing of land surface models: benchmarking model performance, J. Hydrometeor., 16, 1425, https://doi.org/10.1175/JHM-D-14-0158.1, 2015.

Bi, D., Dix, M., Marsland, S., O'Farrell, S., Sullivan, A., Bodman, R., Law, R., Harman, I., Srbinovsky, J., Rashid, H. A., 715 Dobrohotoff, P., Mackallah, C., Yan, H., Hirst, A., Savita, A., Dias, F. B., Woodhouse, M., Fiedler, R., and Heerdegen, A.: Configuration and spin-up of ACCESS-CM2, the new generation Australian Community Climate and Earth System Simulator Coupled Model, Journal of Southern Hemisphere Earth Systems Science, 70, 225-251, https://doi.org/10.1071/ES19040, 2020.

Boé, J.: Interdependency in Multimodel Climate Projections: Component Replication and Result Similarity, Geophysical Research Letters, 45, 2771-2779, https://doi.org/10.1002/2017GL076829, 2018.

720 Boucher, O., Servonnat, J., Albright, A. L., Aumont, O., Balkanski, Y., Bastrikov, V., Bekki, S., Bonnet, R., Bony, S., Bopp, L., Braconnot, P., Brockmann, P., Cadule, P., Caubel, A., Cheruy, F., Codron, F., Cozic, A., Cugnet, D., D'Andrea, F., Davini, P., de Lavergne, C., Denvil, S., Deshayes, J., Devilliers, M., Ducharne, A., Dufresne, J.-L., Dupont, E., Éthé, C., Fairhead, L., Falletti, L., Flavoni, S., Foujols, M.-A., Gardoll, S., Gastineau, G., Ghattas, J., Grandpeix, J.-Y., Guenet, B., Guez, L., E., Guilyardi, E., Guimberteau, M., Hauglustaine, D., Hourdin, F., Idelkadi, A., Joussaume, S., Kageyama, M., Khodri, M., 725 Krinner, G., Lebas, N., Levavasseur, G., Lévy, C., Li, L., Lott, F., Lurton, T., Luyssaert, S., Madec, G., Madeleine, J.-B., Maignan, F., Marchand, M., Marti, O., Mellul, L., Meurdesoif, Y., Mignot, J., Musat, I., Ottlé, C., Peylin, P., Planton, Y., Polcher, J., Rio, C., Rochetin, N., Rousset, C., Sepulchre, P., Sima, A., Swingedouw, D., Thiéblemont, R., Traore, A. K., Vancoppenolle, M., Vial, J., Vialard, J., Viovy, N., and Vuichard, N.: Presentation and Evaluation of the IPSL-CM6A-LR Climate Model, Journal of Advances in Modeling Earth Systems, 12, e2019MS002010, 730 https://doi.org/10.1029/2019MS002010, 2020.

Braganza, K., Karoly, D., Hirst, A., Mann, M., Stott, P., Stouffer, R., and Tett, S.: Simple indices of global climate variability and change: Part I – variability and correlation structure, Climate Dynamics, 20, 491-502, 10.1007/s00382-002-0286-0, 2003.

Brands, S.: Common Error Patterns in the Regional Atmospheric Circulation Simulated by the CMIP Multi-Model Ensemble, Geophysical Research Letters, 49, e2022GL101446, https://doi.org/10.1029/2022GL101446, 2022.

735 Brunner, L., Pendergrass, A. G., Lehner, F., Merrifield, A. L., Lorenz, R., and Knutti, R.: Reduced global warming from CMIP6 projections when weighting models by performance and independence, Earth Syst. Dynam., 11, 995-1012, 10.5194/esd-11-995-2020, 2020.

Cao, J., Wang, B., Yang, Y. M., Ma, L., Li, J., Sun, B., Bao, Y., He, J., Zhou, X., and Wu, L.: The NUIST Earth System Model (NESM) version 3: description and preliminary evaluation, Geosci. Model Dev., 11, 2975-2993, 10.5194/gmd-11-740 2975-2018, 2018.

Chang, C. P., Wang, Z., McBride, J., and Liu, C.-H.: Annual Cycle of Southeast Asia -- Maritime Continent Rainfall and the Asymmetric Monsoon Transition, Journal of Climate 18, 287-301, https://doi.org/10.1175/JCLI-3257.1, 2005.

Chen, C., Sahany, S., Moise, A. F., Chua, X. R., Hassim, M. E., Lim, G., and Prasanna, V.: ENSO–Rainfall Teleconnection over the Maritime Continent Enhances and Shifts Eastward under Warming, Journal of Climate, 36, 4635-4663, 745 https://doi.org/10.1175/JCLI-D-23-0036.1, 2023.

Cherchi, A., Fogli, P. G., Lovato, T., Peano, D., Iovino, D., Gualdi, S., Masina, S., Scoccimarro, E., Materia, S., Bellucci, A., and Navarra, A.: Global Mean Climate and Main Patterns of Variability in the CMCC-CM2 Coupled Model, Journal of Advances in Modeling Earth Systems, 11, 185-209, https://doi.org/10.1029/2018MS001369, 2019.

Contractor, S., Donat, M. G., and Alexander, L. V.: Intensification of the daily wet day rainfall distribution across Australia, 750 Geophysical Research Letters, 45, 8568-8576, 2018.

Contractor, S., Donat, M. G., Alexander, L. V., Ziese, M., Meyer-Christoffer, A., Schneider, U., Rustemeier, E., Becker, A., Durre, I., and Vose, R. S.: Rainfall Estimates on a Gridded Network (REGEN) – a global land-based gridded dataset of daily precipitation from 1950 to 2016, Hydrol. Earth Syst. Sci., 24, 919-943, https://doi.org/10.5194/hess-24-919-2020, 2020.

CORDEX: CORDEX experiment design for dynamical downscaling of CMIP6, https://cordex.org/wp-755 content/uploads/2021/05/CORDEX-CMIP6_exp_design_RCM.pdf, 2021.

D'Arrigo, R. and Wilson, R.: El Nino and Indian Ocean influences on Indonesian drought: implications for forecasting rainfall and crop productivity, International Journal of Climatology: A Journal of the Royal Meteorological Society, 28, 611-616, 2008.

Danabasoglu, G., Lamarque, J.-F., Bacmeister, J., Bailey, D. A., DuVivier, A. K., Edwards, J., Emmons, L. K., Fasullo, J., 760 Garcia, R., Gettelman, A., Hannay, C., Holland, M. M., Large, W. G., Lauritzen, P. H., Lawrence, D. M., Lenaerts, J. T. M., Lindsay, K., Lipscomb, W. H., Mills, M. J., Neale, R., Oleson, K. W., Otto-Bliesner, B., Phillips, A. S., Sacks, W., Tilmes, S., van Kampenhout, L., Vertenstein, M., Bertini, A., Dennis, J., Deser, C., Fischer, C., Fox-Kemper, B., Kay, J. E., Kinnison, D., Kushner, P. J., Larson, V. E., Long, M. C., Mickelson, S., Moore, J. K., Nienhouse, E., Polvani, L., Rasch, P. J., and Strand, W. G.: The Community Earth System Model Version 2 (CESM2), Journal of Advances in Modeling Earth Systems, 12, 765 e2019MS001916, https://doi.org/10.1029/2019MS001916, 2020.

Deng, X., Perkins-Kirkpatrick, S. E., Lewis, S. C., and Ritchie, E. A.: Evaluation of Extreme Temperatures Over Australia in the Historical Simulations of CMIP5 and CMIP6 Models, Earth's Future, 9, e2020EF001902, https://doi.org/10.1029/2020EF001902, 2021.

Desmet, Q. and Ngo-Duc, T.: A novel method for ranking CMIP6 global climate models over the southeast Asian region, International Journal of Climatology, 42, 97-117, https://doi.org/10.1002/joc.7234, 2022.

Di Virgilio, G., Ji, F., Tam, E., Nishant, N., Evans, J. P., Thomas, C., Riley, M. L., Beyer, K., Grose, M. R., Narsey, S., and Delage, F.: Selecting CMIP6 GCMs for CORDEX Dynamical Downscaling: Model Performance, Independence, and Climate Change Signals, Earth's Future, 10, e2021EF002625, https://doi.org/10.1029/2021EF002625, 2022.

Diaconescu, E. P. and Laprise, R.: Can added value be expected in RCM-simulated large scales?, Climate Dynamics, 41, 1769-1800, https://doi.org/10.1007/s00382-012-1649-9, 2013.

Díaz, L. B., Saurral, R. I., and Vera, C. S.: Assessment of South America summer rainfall climatology and trends in a set of global climate models large ensembles, International Journal of Climatology, 41, E59-E77, https://doi.org/10.1002/joc.6643, 2021.

DOE, U. S.: Benchmarking Simulated Precipitation in Earth System Models Workshop Report, DOE/SC-0203, U.S. Department of Energy Office of Science, Biological and Environmental Research (BER) Program, Germantown, Maryland, USA, 2020.

Dommenget, D.: An objective analysis of the observed spatial structure of the tropical Indian Ocean SST variability, Climate Dynamics, 36, 2129-2145, 10.1007/s00382-010-0787-1, 2011.

Donat, M. G., Delgado-Torres, C., De Luca, P., Mahmood, R., Ortega, P., and Doblas-Reyes, F. J.: How Credibly Do CMIP6 Simulations Capture Historical Mean and Extreme Precipitation Changes?, Geophysical Research Letters, 50, e2022GL102466, https://doi.org/10.1029/2022GL102466, 2023.

Dong, T. and Dong, W.: Evaluation of extreme precipitation over Asia in CMIP6 models, Climate Dynamics, 57, 1751-1769, 10.1007/s00382-021-05773-1, 2021.

Döscher, R., Acosta, M., Alessandri, A., Anthoni, P., Arsouze, T., Bergman, T., Bernardello, R., Boussetta, S., Caron, L. P., Carver, G., Castrillo, M., Catalano, F., Cvijanovic, I., Davini, P., Dekker, E., Doblas-Reyes, F. J., Docquier, D., Echevarria, P., Fladrich, U., Fuentes-Franco, R., Gröger, M., v. Hardenberg, J., Hieronymus, J., Karami, M. P., Keskinen, J. P., Koenigk, T., Makkonen, R., Massonnet, F., Ménégoz, M., Miller, P. A., Moreno-Chamarro, E., Nieradzik, L., van Noije, T., Nolan, P., O'Donnell, D., Ollinaho, P., van den Oord, G., Ortega, P., Prims, O. T., Ramos, A., Reerink, T., Rousset, C., Ruprich-Robert, Y., Le Sager, P., Schmith, T., Schrödner, R., Serva, F., Sicardi, V., Sloth Madsen, M., Smith, B., Tian, T., Tourigny, E., Uotila, P., Vancoppenolle, M., Wang, S., Wårlind, D., Willén, U., Wyser, K., Yang, S., Yepes-Arbós, X., and Zhang, Q.: The EC-Earth3 Earth system model for the Coupled Model Intercomparison Project 6, Geosci. Model Dev., 15, 2973-3020, 10.5194/gmd-15-2973-2022, 2022.

Douville, H., Raghavan, K., Renwick, J., Allan, R. P., Arias, P. A., Barlow, M., Cerezo-Mota, R., Cherchi, A., Gan, T. Y., Gergis, J., Jiang, D., Khan, A., Pokam Mba, W., Rosenfeld, D., Tierney, J., and Zolina, O.: Water Cycle Changes, in: Climate Change 2021: The Physical Science Basis. Contribution of Working Group I to the Sixth Assessment Report of the Intergovernmental Panel on Climate Change, edited by: Masson-Delmotte, V., Zhai, P., Pirani, A., Connors, S. L., Péan, C., Berger, S., Caud, N., Chen, Y., Goldfarb, L., Gomis, M. I., Huang, M., Leitzell, K., Lonnoy, E., Matthews, J. B. R., Maycock, T. K., Waterfield, T., Yelekçi, O., Yu, R., and Zhou, B., Cambridge University Press, Cambridge, United Kingdom and New York, NY, USA, 1055–1210, 10.1017/9781009157896.010, 2021.

Dunne, J. P., Horowitz, L. W., Adcroft, A. J., Ginoux, P., Held, I. M., John, J. G., Krasting, J. P., Malyshev, S., Naik, V., Paulot, F., Shevliakova, E., Stock, C. A., Zadeh, N., Balaji, V., Blanton, C., Dunne, K. A., Dupuis, C., Durachta, J., Dussin, R., Gauthier, P. P. G., Griffies, S. M., Guo, H., Hallberg, R. W., Harrison, M., He, J., Hurlin, W., McHugh, C., Menzel, R., Milly, P. C. D., Nikonov, S., Paynter, D. J., Ploshay, J., Radhakrishnan, A., Rand, K., Reichl, B. G., Robinson, T.,

Schwarzkopf, D. M., Sentman, L. T., Underwood, S., Vahlenkamp, H., Winton, M., Wittenberg, A. T., Wyman, B., Zeng, Y.,
810 and Zhao, M.: The GFDL Earth System Model Version 4.1 (GFDL-ESM 4.1): Overall Coupled Model Description and
Simulation Characteristics, Journal of Advances in Modeling Earth Systems, 12, e2019MS002015,
https://doi.org/10.1029/2019MS002015, 2020.

Evans, J., Virgilio, G., Hirsch, A., Hoffmann, P., Remedio, A. R., Ji, F., Rockel, B., and Coppola, E.: The CORDEX-
Australasia ensemble: evaluation and future projections, Climate Dynamics, 57, 10.1007/s00382-020-05459-0, 2021.

815 Funk, C., Peterson, P., Landsfeld, M., Pedreros, D., Verdin, J., Shukla, S., Husak, G., Rowland, J., Harrison, L., Hoell, A., and
Michaelsen, J.: The climate hazards infrared precipitation with stations—a new environmental record for monitoring extremes,
Scientific Data, 2, 150066, https://doi.org/10.1038/sdata.2015.66, 2015.

Gibson, P. B., Perkins-Kirkpatrick, S. E., Alexander, L. V., and Fischer, E. M.: Comparing Australian heat waves in the CMIP5
models through cluster analysis, Journal of Geophysical Research: Atmospheres, 122, 3266-3281,
820 https://doi.org/10.1002/2016JD025878, 2017.

Gibson, P. B., Rampal, N., Dean, S. M., and Morgenstern, O.: Storylines for Future Projections of Precipitation Over New
Zealand in CMIP6 Models, Journal of Geophysical Research: Atmospheres, 129, e2023JD039664,
https://doi.org/10.1029/2023JD039664, 2024.

Giorgi, F. and Gao, X.: Regional earth system modeling: review and future directions, Atmospheric and Oceanic Science
825 Letters, 11, 1-9, https://doi.org/10.1080/16742834.2018.1452520, 2018.

Giorgi, F., Jones, C., and Asrar, G.: Addressing climate information needs at the regional level: The CORDEX framework,
WMO Bull, 53, 2008.

Giorgi, F., Coppola, E., Teichmann, C., and Jacob, D.: Editorial for the CORDEX-CORE Experiment I Special Issue, Climate
Dynamics, 57, 1265-1268, https://doi.org/10.1007/s00382-021-05902-w, 2021.

830 Grose, M. R., Narsey, S., Trancoso, R., Mackallah, C., Delage, F., Dowdy, A., Di Virgilio, G., Watterson, I., Dobrohotoff, P.,
Rashid, H. A., Rauniyar, S., Henley, B., Thatcher, M., Syktus, J., Abramowitz, G., Evans, J. P., Su, C.-H., and Takbash, A.: A
CMIP6-based multi-model downscaling ensemble to underpin climate change services in Australia, Climate Services, 30,
100368, https://doi.org/10.1016/j.cliser.2023.100368, 2023.

Haylock, M. and McBride, J.: Spatial coherence and predictability of Indonesian wet season rainfall, Journal of Climate, 14,
835 3882-3887, https://doi.org/10.1175/1520-0442(2001)014<3882:SCAPOI>2.0.CO;2, 2001.

Held, I. M., Guo, H., Adcroft, A., Dunne, J. P., Horowitz, L. W., Krasting, J., Shevliakova, E., Winton, M., Zhao, M., Bushuk,
M., Wittenberg, A. T., Wyman, B., Xiang, B., Zhang, R., Anderson, W., Balaji, V., Donner, L., Dunne, K., Durachta, J.,
Gauthier, P. P. G., Ginoux, P., Golaz, J. C., Griffies, S. M., Hallberg, R., Harris, L., Harrison, M., Hurlin, W., John, J., Lin, P.,
Lin, S. J., Malyshev, S., Menzel, R., Milly, P. C. D., Ming, Y., Naik, V., Paynter, D., Paulot, F., Ramaswamy, V., Reichl, B.,
840 Robinson, T., Rosati, A., Seman, C., Silvers, L. G., Underwood, S., and Zadeh, N.: Structure and Performance of GFDL's
CM4.0 Climate Model, Journal of Advances in Modeling Earth Systems, 11, 3691-3727,
https://doi.org/10.1029/2019MS001829, 2019.

Herger, N., Abramowitz, G., Sherwood, S., Knutti, R., Angélil, O., and Sisson, S. A.: Ensemble optimisation, multiple
constraints and overconfidence: a case study with future Australian precipitation change, Climate Dynamics, 53, 1581-1596,
845 10.1007/s00382-019-04690-8, 2019.

Hersbach, H., Bell, B., Berrisford, P., Hirahara, S., Horányi, A., Muñoz-Sabater, J., Nicolas, J., Peubey, C., Radu, R., Schepers, D., Simmons, A., Soci, C., Abdalla, S., Abellan, X., Balsamo, G., Bechtold, P., Biavati, G., Bidlot, J., Bonavita, M., De Chiara, G., Dahlgren, P., Dee, D., Diamantakis, M., Dragani, R., Flemming, J., Forbes, R., Fuentes, M., Geer, A., Haimberger, L., Healy, S., Hogan, R. J., Hólm, E., Janisková, M., Keeley, S., Laloyaux, P., Lopez, P., Lupu, C., Radnoti, G., de Rosnay, P., Rozum, I., Vamborg, F., Villaume, S., and Thépaut, J.-N.: The ERA5 global reanalysis, Quarterly Journal of the Royal Meteorological Society, 146, 1999-2049, https://doi.org/10.1002/qj.3803, 2020.

Huang, B., Liu, C., Banzon, V., Freeman, E., Graham, G., Hankins, B., Smith, T., and Zhang, H.-M.: Improvements of the Daily Optimum Interpolation Sea Surface Temperature (DOISST) Version 2.1, Journal of Climate, 34, 2923-2939, https://doi.org/10.1175/JCLI-D-20-0166.1, 2021.

Huang, B., Thorne, P. W., Banzon, V. F., Boyer, T., Chepurin, G., Lawrimore, J. H., Menne, M. J., Smith, T. M., Vose, R. S., and Zhang, H.-M.: Extended Reconstructed Sea Surface Temperature, Version 5 (ERSSTv5): Upgrades, Validations, and Intercomparisons, Journal of Climate, 30, 8179-8205, https://doi.org/10.1175/JCLI-D-16-0836.1, 2017.

Ignacio-Reardon, S. and Luo, J.-j.: Evaluation of the Performance of CMIP6 Climate Models in Simulating Rainfall over the Philippines, Atmosphere, 14, 1459, 10.3390/atmos14091459, 2023.

IPCC: Summary for Policymakers, in: Climate Change 2022 - Mitigation of Climate Change: Working Group III Contribution to the Sixth Assessment Report of the Intergovernmental Panel on Climate Change, edited by: Change, I. P. o. C., Cambridge University Press, Cambridge, UK and New York, NY, USA, 1-2, 10.1017/9781009157926.001., 2022.

IPCC: Summary for Policymakers in: Climate Change 2023: Synthesis Report, edited by: Contribution of Working Groups I, I. a. I. t. t. S. A. R. o. t. I. P. o. C. C. C. W. T., H. Lee and J. Romero (eds.)], IPCC, Geneva, Switzerland, 1-34, 0.59327/IPCC/AR6-9789291691647.001, 2023.

Isphording, R. N.: ni422/aus_precip_benchmarking: Updated - Benchmarking Precipitation in Regional Climate Models: Jupyter Notebooks (Python) for the Minimum Standard Metrics and two simple example applications (v1.1) [dataset], https://doi.org/10.5281/zenodo.10668767, 2024.

Isphording, R. N., Alexander, L. V., Bador, M., Green, D., Evans, J. P., and Wales, S.: A Standardized Benchmarking Framework to Assess Downscaled Precipitation Simulations, Journal of Climate, 37, 1089-1110, https://doi.org/10.1175/JCLI-D-23-0317.1, 2024.

Jacob, D., Teichmann, C., Sobolowski, S., Katragkou, E., Anders, I., Belda, M., Benestad, R., Boberg, F., Buonomo, E., Cardoso, R. M., Casanueva, A., Christensen, O. B., Christensen, J. H., Coppola, E., De Cruz, L., Davin, E. L., Dobler, A., Domínguez, M., Fealy, R., Fernandez, J., Gaertner, M. A., García-Díez, M., Giorgi, F., Gobiet, A., Goergen, K., Gómez-Navarro, J. J., Alemán, J. J. G., Gutiérrez, C., Gutiérrez, J. M., Güttler, I., Haensler, A., Halenka, T., Jerez, S., Jiménez-Guerrero, P., Jones, R. G., Keuler, K., Kjellström, E., Knist, S., Kotlarski, S., Maraun, D., van Meijgaard, E., Mercogliano, P., Montávez, J. P., Navarra, A., Nikulin, G., de Noblet-Ducoudré, N., Panitz, H.-J., Pfeifer, S., Piazza, M., Pichelli, E., Pietikäinen, J.-P., Prein, A. F., Preuschmann, S., Rechid, D., Rockel, B., Romera, R., Sánchez, E., Sieck, K., Soares, P. M. M., Somot, S., Srnec, L., Sørland, S. L., Termonia, P., Truhetz, H., Vautard, R., Warrach-Sagi, K., and Wulfmeyer, V.: Regional climate downscaling over Europe: perspectives from the EURO-CORDEX community, Regional Environmental Change, 20, 51, 10.1007/s10113-020-01606-9, 2020.

Jones, P. W.: First- and Second-Order Conservative Remapping Schemes for Grids in Spherical Coordinates, Mon. Wea. Rev., 127, 2204–2210, https://doi.org/10.1175/1520-0493(1999), 1999.

Juneng, L. and Tangang, F. T.: Evolution of ENSO-related rainfall anomalies in Southeast Asia region and its relationship with atmosphere–ocean variations in Indo-Pacific sector, Climate Dynamics, 25, 337-350, 2005.

Juneng, L., Tangang, F., Chung, J. X., Ngai, S. T., Teh, T. W., Narisma, G., Cruz, F., Phan-Van, T., Ngo-Duc, T., Santisirisomboon, J., Singhruck, P., Gunawan, D., and Aldrian, E.: Sensitivity of Southeast Asia rainfall simulations to cumulus and air–sea flux parameterizations in RegCM4, Climate Research, 69, https://doi.org/10.3354/cr01386, 2016.

Kamworapan, S., Bich Thao, P. T., Gheewala, S. H., Pimonsree, S., and Prueksakorn, K.: Evaluation of CMIP6 GCMs for simulations of temperature over Thailand and nearby areas in the early 21st century, Heliyon, 7, e08263, https://doi.org/10.1016/j.heliyon.2021.e08263, 2021.

Kendall: Rank Correlation Coefficient, in, Springer New York, New York, NY, 278-281, https://doi.org/10.1007/978-0-387-32833-1_211, 1975.

Kim, Y.-H., Min, S.-K., Zhang, X., Sillmann, J., and Sandstad, M.: Evaluation of the CMIP6 multi-model ensemble for climate extreme indices, Weather and Climate Extremes, 29, 100269, https://doi.org/10.1016/j.wace.2020.100269, 2020.

Knutti, R. and Sedláček, J.: Robustness and uncertainties in the new CMIP5 climate model projections, Nature Climate Change, 3, 369-373, 10.1038/nclimate1716, 2013.

Knutti, R., Furrer, R., Tebaldi, C., Cermak, J., and Meehl, G. A.: Challenges in Combining Projections from Multiple Climate Models, Journal of Climate, 23, 2739-2758, https://doi.org/10.1175/2009jcli3361.1, 2010.

Langenbrunner, B. and Neelin, J. D.: Analyzing ENSO Teleconnections in CMIP Models as a Measure of Model Fidelity in Simulating Precipitation, Journal of Climate, 26, 4431-4446, https://doi.org/10.1175/JCLI-D-12-00542.1, 2013.

Liu, Y. L., Alexander, L. V., Evans, J. P., and Thatcher, M.: Sensitivity of Australian rainfall to driving SST datasets in a variable-resolution global atmospheric model, http://dx.doi.org/10.22541/essoar.170913616.69157157/v1, 2024.

Maraun, D. and Widmann, M.: Statistical downscaling and bias correction for climate research, Cambridge University Press, https://doi.org/10.1017/9781107588783, 2018.

Masson, D. and Knutti, R.: Spatial-Scale Dependence of Climate Model Performance in the CMIP3 Ensemble, Journal of Climate, 24, 2680-2692, https://doi.org/10.1175/2011JCLI3513.1, 2011.

Mauritsen, T., Bader, J., Becker, T., Behrens, J., Bittner, M., Brokopf, R., Brovkin, V., Claussen, M., Crueger, T., Esch, M., Fast, I., Fiedler, S., Fläschner, D., Gayler, V., Giorgetta, M., Goll, D. S., Haak, H., Hagemann, S., Hedemann, C., Hohenegger, C., Ilyina, T., Jahns, T., Jimenéz-de-la-Cuesta, D., Jungclaus, J., Kleinen, T., Kloster, S., Kracher, D., Kinne, S., Kleberg, D., Lasslop, G., Kornblueh, L., Marotzke, J., Matei, D., Meraner, K., Mikolajewicz, U., Modali, K., Möbis, B., Müller, W. A., Nabel, J. E. M. S., Nam, C. C. W., Notz, D., Nyawira, S.-S., Paulsen, H., Peters, K., Pincus, R., Pohlmann, H., Pongratz, J., Popp, M., Raddatz, T. J., Rast, S., Redler, R., Reick, C. H., Rohrschneider, T., Schemann, V., Schmidt, H., Schnur, R., Schulzweida, U., Six, K. D., Stein, L., Stemmler, I., Stevens, B., von Storch, J.-S., Tian, F., Voigt, A., Vrese, P., Wieners, K.-H., Wilkenskjeld, S., Winkler, A., and Roeckner, E.: Developments in the MPI-M Earth System Model version 1.2 (MPI-ESM1.2) and Its Response to Increasing CO2, Journal of Advances in Modeling Earth Systems, 11, 998-1038, https://doi.org/10.1029/2018MS001400, 2019.

McKenna, S., Santoso, A., Gupta, A. S., Taschetto, A. S., and Cai, W.: Indian Ocean Dipole in CMIP5 and CMIP6: characteristics, biases, and links to ENSO, Scientific Reports, 10, 11500, 10.1038/s41598-020-68268-9, 2020.

McSweeney, C. F., Jones, R. G., and Booth, B. B. B.: Selecting Ensemble Members to Provide Regional Climate Change Information, Journal of Climate, 25, 7100-7121, https://doi.org/10.1175/JCLI-D-11-00526.1, 2012.

McSweeney, C. F., Jones, R. G., Lee, R. W., and Rowell, D. P.: Selecting CMIP5 GCMs for downscaling over multiple regions, Climate Dynamics, 44, 3237-3260, https://doi.org/10.1007/s00382-014-2418-8, 2015.

925 Meehl, G. A., Boer, G. J., Covey, C., Latif, M., and Stouffer, R. J.: The Coupled Model Intercomparison Project (CMIP), Bulletin of the American Meteorological Society, 81, 313-318, https://doi.org/10.1175/1520-0477(2000)081<0313:Tcmipc>2.3.Co;2, 2000.

Meyers, G., McIntosh, P., Pigot, L., and Pook, M.: The Years of El Niño, La Niña, and Interactions with the Tropical Indian Ocean, Journal of Climate, 20, 2872-2880, https://doi.org/10.1175/JCLI4152.1, 2007.

Mote, P., Brekke, L., Duffy, P. B., and Maurer, E.: Guidelines for constructing climate scenarios, Eos, Transactions American 930 Geophysical Union, 92, 257-258, https://doi.org/10.1029/2011EO310001, 2011.

Nearing, G. S., Ruddell, B. L., Clark, M. P., Nijssen, B., and Peters-Lidard, C.: Benchmarking and Process Diagnostics of Land Models, Journal of Hydrometeorology, 19, 1835-1852, https://doi.org/10.1175/JHM-D-17-0209.1, 2018.

Nguyen, P.-L., Bador, M., Alexander, L. V., and Lane, T. P.: Selecting regional climate models based on their skill could give more credible precipitation projections over the complex Southeast Asia region, Climate Dynamics, 61, 3431-3452, 935 10.1007/s00382-023-06751-5, 2023.

Nguyen, P.-L., Bador, M., Alexander, L. V., Lane, T. P., and Funk, C. C.: On the Robustness of Annual Daily Precipitation Maxima Estimates Over Monsoon Asia, Frontiers in Climate, 2, https://doi.org/10.3389/fclim.2020.578785, 2020.

Nguyen, P.-L., Bador, M., Alexander, L. V., Lane, T. P., and Ngo-Duc, T.: More intense daily precipitation in CORDEX-SEA regional climate models than their forcing global climate models over Southeast Asia, International Journal of Climatology, 940 n/a, https://doi.org/10.1002/joc.7619, 2022.

Nguyen-Duy, T., Ngo-Duc, T., and Desmet, Q.: Performance evaluation and ranking of CMIP6 global climate models over Vietnam, Journal of Water and Climate Change, 14, 1831-1846, 10.2166/wcc.2023.454, 2023.

Ossó, A., Craig, P., and Allan, R. P.: An assessment of CMIP6 climate signals and biases in temperature, precipitation and soil moisture over Europe, International Journal of Climatology, 43, 5698-5719, https://doi.org/10.1002/joc.8169, 2023.

945 Overland, J. E., Wang, M., Bond, N. A., Walsh, J. E., Kattsov, V. M., and Chapman, W. L.: Considerations in the Selection of Global Climate Models for Regional Climate Projections: The Arctic as a Case Study, Journal of Climate, 24, 1583-1597, https://doi.org/10.1175/2010JCLI3462.1, 2011.

Palmer, T. E., McSweeney, C. F., Booth, B. B. B., Priestley, M. D. K., Davini, P., Brunner, L., Borchert, L., and Menary, M. B.: Performance-based sub-selection of CMIP6 models for impact assessments in Europe, Earth Syst. Dynam., 14, 457-483, 950 10.5194/esd-14-457-2023, 2023.

Park, S., Shin, J., Kim, S., Oh, E., and Kim, Y.: Global Climate Simulated by the Seoul National University Atmosphere Model Version 0 with a Unified Convection Scheme (SAM0-UNICON), Journal of Climate, 32, 2917-2949, https://doi.org/10.1175/JCLI-D-18-0796.1, 2019.

Perry, S. J., McGregor, S., Sen Gupta, A., England, M. H., and Maher, N.: Projected late 21st century changes to the regional 955 impacts of the El Niño-Southern Oscillation, Climate Dynamics, 54, 395-412, 10.1007/s00382-019-05006-6, 2020.

Pimonsree, S., Kamworapan, S., Gheewala, S. H., Thongbhakdi, A., and Prueksakorn, K.: Evaluation of CMIP6 GCMs performance to simulate precipitation over Southeast Asia, Atmospheric Research, 282, 106522, https://doi.org/10.1016/j.atmosres.2022.106522, 2023.

960 Planton, Y. Y., Guilyardi, E., Wittenberg, A. T., Lee, J., Gleckler, P. J., Bayr, T., McGregor, S., McPhaden, M. J., Power, S., Roehrig, R., Vialard, J., and Voldoire, A.: Evaluating Climate Models with the CLIVAR 2020 ENSO Metrics Package, Bulletin of the American Meteorological Society, 102, E193-E217, https://doi.org/10.1175/BAMS-D-19-0337.1, 2021.

Power, S. B. and Delage, F. P. D.: El Niño–Southern Oscillation and Associated Climatic Conditions around the World during the Latter Half of the Twenty-First Century, Journal of Climate, 31, 6189-6207, https://doi.org/10.1175/JCLI-D-18-0138.1, 2018.

965 Qian, J.-H., Robertson, A. W., and Moron, V.: Diurnal cycle in different weather regimes and rainfall variability over Borneo associated with ENSO, Journal of Climate, 26, 1772-1790, https://doi.org/10.1175/JCLI-D-12-00178.1, 2013.

Rayner, N. A., Parker, D. E., Horton, E. B., Folland, C. K., Alexander, L. V., Rowell, D. P., Kent, E. C., and Kaplan, A.: Global analyses of sea surface temperature, sea ice, and night marine air temperature since the late nineteenth century, Journal of Geophysical Research: Atmospheres, 108, https://doi.org/10.1029/2002JD002670, 2003.

970 Ridder, N. N., Pitman, A. J., and Ukkola, A. M.: Do CMIP6 Climate Models Simulate Global or Regional Compound Events Skillfully?, Geophysical Research Letters, 48, e2020GL091152, https://doi.org/10.1029/2020GL091152, 2021.

Rousseeuw, P. J.: Silhouettes: A graphical aid to the interpretation and validation of cluster analysis, Journal of Computational and Applied Mathematics, 20, 53-65, https://doi.org/10.1016/0377-0427(87)90125-7, 1987.

Saji, N. H., Goswami, B. N., Vinayachandran, P. N., and Yamagata, T.: A dipole mode in the tropical Indian Ocean, Nature, 975 401, 360-363, 10.1038/43854, 1999.

Schamm, K., Ziese, M., Becker, A., Finger, P., Meyer-Christoffer, A., Schneider, U., Schröder, M., and Stender, P.: Global gridded precipitation over land: a description of the new GPCC First Guess Daily product, Earth Syst. Sci. Data, 6, 49-60, https://doi.org/10.5194/essd-6-49-2014, 2014.

Seland, Ø., Bentsen, M., Olivié, D., Toniazzo, T., Gjermundsen, A., Graff, L. S., Debernard, J. B., Gupta, A. K., He, Y. C., 980 Kirkevåg, A., Schwinger, J., Tjiputra, J., Aas, K. S., Bethke, I., Fan, Y., Griesfeller, J., Grini, A., Guo, C., Ilicak, M., Karset, I. H. H., Landgren, O., Liakka, J., Moseid, K. O., Nummelin, A., Spensberger, C., Tang, H., Zhang, Z., Heinze, C., Iversen, T., and Schulz, M.: Overview of the Norwegian Earth System Model (NorESM2) and key climate response of CMIP6 DECK, historical, and scenario simulations, Geosci. Model Dev., 13, 6165-6200, 10.5194/gmd-13-6165-2020, 2020.

Sellar, A. A., Jones, C. G., Mulcahy, J. P., Tang, Y., Yool, A., Wiltshire, A., O'Connor, F. M., Stringer, M., Hill, R., Palmieri, 985 J., Woodward, S., de Mora, L., Kuhlbrodt, T., Rumbold, S. T., Kelley, D. I., Ellis, R., Johnson, C. E., Walton, J., Abraham, N. L., Andrews, M. B., Andrews, T., Archibald, A. T., Berthou, S., Burke, E., Blockley, E., Carslaw, K., Dalvi, M., Edwards, J., Folberth, G. A., Gedney, N., Griffiths, P. T., Harper, A. B., Hendry, M. A., Hewitt, A. J., Johnson, B., Jones, A., Jones, C. D., Keeble, J., Liddicoat, S., Morgenstern, O., Parker, R. J., Predoi, V., Robertson, E., Siahaan, A., Smith, R. S., Swaminathan, R., Woodhouse, M. T., Zeng, G., and Zerroukat, M.: UKESM1: Description and Evaluation of the U.K. Earth System Model, 990 Journal of Advances in Modeling Earth Systems, 11, 4513-4558, https://doi.org/10.1029/2019MS001739, 2019.

Shukla, R. P., Tripathi, K. C., Pandey, A. C., and Das, I.: Prediction of Indian summer monsoon rainfall using Niño indices: a neural network approach, Atmospheric Research, 102, 99-109, 2011.

Sobolowski, S., Somot, S., Fernandez, J., Evin, G., Maraun, D., Kotlarski, S., Jury, M., Benestad, R. E., Teichmann, C., Christensen, O. B., Bülow, K., Buonomo, E., Katragkou, E., Steger, C., Sørland, S., Nikulin, G., McSweeney, C., Dobler, A., Palmer, T., Wilcke, R., Boé, J., Brunner, L., Ribes, A., Qasmi, S., Nabat, P., Sevault, F., Oudar, T., and Brands, S.: EURO-CORDEX CMIP6 GCM Selection & Ensemble Design: Best Practices and Recommendations, Zenodo, https://doi.org/10.5281/zenodo.7673400, 2023.

Supari, S., Tangang, F., Salimun, E., Aldrian, E., Sopaheluwakan, A., and Juneng, L.: ENSO modulation of seasonal rainfall and extremes in Indonesia, Climate Dynamics, 51, 10.1007/s00382-017-4028-8, 2018.

Tangang, F., Chung, J. X., Juneng, L., Supari, Salimun, E., Ngai, S. T., Jamaluddin, A. F., Mohd, M. S. F., Cruz, F., Narisma, G., Santisirisomboon, J., Ngo-Duc, T., Van Tan, P., Singhruck, P., Gunawan, D., Aldrian, E., Sopaheluwakan, A., Grigory, N., Remedio, A. R. C., Sein, D. V., Hein-Griggs, D., McGregor, J. L., Yang, H., Sasaki, H., and Kumar, P.: Projected future changes in rainfall in Southeast Asia based on CORDEX–SEA multi-model simulations, Climate Dynamics, 55, 1247-1267, https://doi.org/10.1007/s00382-020-05322-2, 2020.

Taschetto, A. S., Gupta, A. S., Jourdain, N. C., Santoso, A., Ummenhofer, C. C., and England, M. H.: Cold Tongue and Warm Pool ENSO Events in CMIP5: Mean State and Future Projections, Journal of Climate, 27, 2861-2885, https://doi.org/10.1175/JCLI-D-13-00437.1, 2014.

Tatebe, H., Ogura, T., Nitta, T., Komuro, Y., Ogochi, K., Takemura, T., Sudo, K., Sekiguchi, M., Abe, M., Saito, F., Chikira, M., Watanabe, S., Mori, M., Hirota, N., Kawatani, Y., Mochizuki, T., Yoshimura, K., Takata, K., O'Ishi, R., Yamazaki, D., Suzuki, T., Kurogi, M., Kataoka, T., Watanabe, M., and Kimoto, M.: Description and basic evaluation of simulated mean state, internal variability, and climate sensitivity in MIROC6, Geosci. Model Dev., 12, 2727-2765, 10.5194/gmd-12-2727-2019, 2019.

Trenberth, K. E. and Hoar, T. J.: El Niño and climate change, Geophysical Research Letters, 24, 3057-3060, https://doi.org/10.1029/97GL03092, 1997.

Voldoire, A., Saint-Martin, D., Sénési, S., Decharme, B., Alias, A., Chevallier, M., Colin, J., Guérémy, J.-F., Michou, M., Moine, M.-P., Nabat, P., Roehrig, R., Salas y Mélia, D., Séférian, R., Valcke, S., Beau, I., Belamari, S., Berthet, S., Cassou, C., Cattiaux, J., Deshayes, J., Douville, H., Ethé, C., Franchistéguy, L., Geoffroy, O., Lévy, C., Madec, G., Meurdesoif, Y., Msadek, R., Ribes, A., Sanchez-Gomez, E., Terray, L., and Waldman, R.: Evaluation of CMIP6 DECK Experiments With CNRM-CM6-1, Journal of Advances in Modeling Earth Systems, 11, 2177-2213, https://doi.org/10.1029/2019MS001683, 2019.

Volodin, E. M., Mortikov, E. V., Kostrykin, S. V., Galin, V. Y., Lykosov, V. N., Gritsun, A. S., Diansky, N. A., Gusev, A. V., and Yakovlev, N. G.: Simulation of modern climate with the new version of the INM RAS climate model, Izvestiya, Atmospheric and Oceanic Physics, 53, 142-155, 10.1134/S0001433817020128, 2017.

Wang, B., Luo, X., and Liu, J.: How Robust is the Asian Precipitation–ENSO Relationship during the Industrial Warming Period (1901–2017)?, Journal of Climate, 33, 2779-2792, https://doi.org/10.1175/JCLI-D-19-0630.1, 2020.

Wang, Y.-C., Hsu, H.-H., Chen, C.-A., Tseng, W.-L., Hsu, P.-C., Lin, C.-W., Chen, Y.-L., Jiang, L.-C., Lee, Y.-C., Liang, H.-C., Chang, W.-M., Lee, W.-L., and Shiu, C.-J.: Performance of the Taiwan Earth System Model in Simulating Climate Variability Compared With Observations and CMIP6 Model Simulations, Journal of Advances in Modeling Earth Systems, 13, e2020MS002353, https://doi.org/10.1029/2020MS002353, 2021a.

Wang, Z., Zhan, C., Ning, L., and Guo, H.: Evaluation of global terrestrial evapotranspiration in CMIP6 models, Theoretical and Applied Climatology, 143, 521-531, https://doi.org/10.1007/s00704-020-03437-4, 2021b.

Wu, T., Lu, Y., Fang, Y., Xin, X., Li, L., Li, W., Jie, W., Zhang, J., Liu, Y., Zhang, L., Zhang, F., Zhang, Y., Wu, F., Li, J., Chu, M., Wang, Z., Shi, X., Liu, X., Wei, M., Huang, A., Zhang, Y., and Liu, X.: The Beijing Climate Center Climate System Model (BCC-CSM): the main progress from CMIP5 to CMIP6, Geosci. Model Dev., 12, 1573-1600, 10.5194/gmd-12-1573-2019, 2019.

Xu, J., Koldunov, N. V., Xu, M., Zhu, X., Fraedrich, K., Jiang, X., Zhu, S., and Zhi, X.: Impacts of Indian Ocean Dipole–Like SST on Rice Yield Anomalies in Jiangsu Province, Frontiers in Earth Science, 8, 690, https://doi.org/10.3389/feart.2020.568365, 2021.

Yatagai, A., Kamiguchi, K., Arakawa, O., Hamada, A., Yasutomi, N., and Kitoh, A.: APHRODITE: Constructing a Long-Term Daily Gridded Precipitation Dataset for Asia Based on a Dense Network of Rain Gauges, Bulletin of the American Meteorological Society, 93, 1401-1415, https://doi.org/10.1175/BAMS-D-11-00122.1, 2012.

Yukimoto, S., Kawai, H., Koshiro, T., Oshima, N., Yoshida, K., Urakawa, S., Tsujino, H., Deushi, M., Tanaka, T., Hosaka, M., Yabu, S., Yoshimura, H., Shindo, E., Mizuta, R., Obata, A., Adachi, Y., and Ishii, M.: The Meteorological Research Institute Earth System Model Version 2.0, MRI-ESM2.0: Description and Basic Evaluation of the Physical Component, Journal of the Meteorological Society of Japan. Ser. II, 97, 931-965, 10.2151/jmsj.2019-051, 2019.

Zheng, X., Li, Q., Zhou, T., Tang, Q., Van Roekel, L. P., Golaz, J. C., Wang, H., and Cameron-Smith, P.: Description of historical and future projection simulations by the global coupled E3SMv1.0 model as used in CMIP6, Geosci. Model Dev., 15, 3941-3967, 10.5194/gmd-15-3941-2022, 2022.

Ziehn, T., Chamberlain, M. A., Law, R. M., Lenton, A., Bodman, R. W., Dix, M., Stevens, L., Wang, Y.-P., and Srbinovsky, J.: The Australian Earth System Model: ACCESS-ESM1.5, Journal of Southern Hemisphere Earth Systems Science, 70, 193-214, https://doi.org/10.1071/ES19035, 2020.